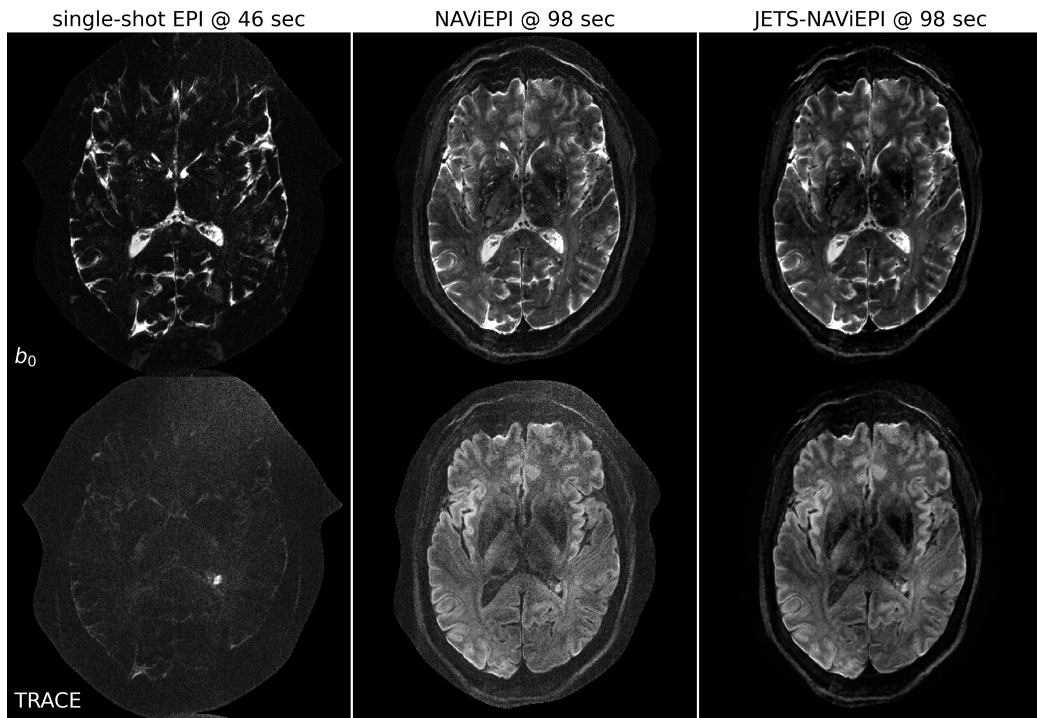


Graphical Abstract

Accelerated Diffusion Weighted Magnetic Resonance Imaging at 7 T: Joint Reconstruction for Shift-Encoded Navigator-based Interleaved Echo Planar Imaging (JETS-NAViEPI)

Zhengguo Tan, Patrick Alexander Liebig, Robin Martin Heidemann, Frederik Bernd Laun, Florian Knoll

3-scan trace acquisition with voxel size 0.5 X 0.5 X 2.0 mm³



Highlights

Accelerated Diffusion Weighted Magnetic Resonance Imaging at 7 T: Joint Reconstruction for Shift-Encoded Navigator-based Interleaved Echo Planar Imaging (JETS-NAViEPI)

Zhengguo Tan, Patrick Alexander Liebig, Robin Martin Heidemann, Frederik Bernd Laun, Florian Knoll

- Navigator-based interleaved EPI acquisition with minimal distortion mismatch between echoes
- Novel accelerated diffusion acquisition with shifted phase encoding among diffusion directions for complementary k - q -space sampling at 7 T
- Generalized joint k - q -slice diffusion-weighted image reconstruction with overlapping locally low-rank regularization
- Efficient simultaneous multi-slice (SMS) image reconstruction
- 3-scan trace acquisition with the voxel size $0.5 \times 0.5 \times 2.0 \text{ mm}^3$ and 60 slices at 1.5 min

Accelerated Diffusion Weighted Magnetic Resonance Imaging at 7 T: Joint Reconstruction for Shift-Encoded Navigator-based Interleaved Echo Planar Imaging (JETS-NAViEPI)

Zhengguo Tan^a, Patrick Alexander Liebig^b, Robin Martin Heidemann^b,
Frederik Bernd Laun^c, Florian Knoll^a

^a*Department Artificial Intelligence in Biomedical Engineering (AIBE),
Friedrich-Alexander University of Erlangen-Nuremberg, Erlangen, Germany*

^b*Siemens Healthcare GmbH, Erlangen, Germany*

^c*Institute of Radiology, University Hospital Erlangen, Friedrich-Alexander University of Erlangen-Nuremberg, Erlangen, Germany*

Abstract

The pursuit of high spatial-angular-temporal resolution for in vivo diffusion-weighted magnetic resonance imaging (DW-MRI) at ultra-high field strength (7 T and above) is important in understanding brain microstructure and function. Such pursuit, however, faces several technical challenges. First, increased off-resonance and shorter T_2 relaxation require faster echo train readouts. Second, existing high-resolution DW-MRI techniques usually employ in-plane fully-sampled multi-shot EPI, which not only prolongs the scan time but also induces a high specific absorption rate (SAR) at 7 T. To address these challenges, we develop in this work navigator-based interleaved EPI (NAViEPI) which enforces the same effective echo spacing (ESP) between the imaging and the navigator echo. First, NAViEPI renders no distortion mismatch between the two echoes, and thus simplifies shot-to-shot phase variation correction. Second, NAViEPI allows for a large number of shots

(e.g. > 4) with undersampled iEPI acquisition, thereby rendering clinically-feasible high-resolution sub-millimeter protocols. To retain signal-to-noise ratio (SNR) and to reduce undersampling artifacts, we developed a k_y -shift encoding among diffusion encodings to explore complementary k - q -space sampling. Moreover, we developed a novel joint reconstruction with overlapping locally low-rank regularization generalized to the multi-band multi-shot acquisition at 7 T (dubbed JETS-NAViEPI). Our method was demonstrated with experimental results covering 1 mm isotropic resolution multi b -value DWI and sub-millimeter in-plane resolution fast TRACE acquisition.

Keywords: Diffusion-weighted magnetic resonance imaging, Echo planar imaging, Navigator, Ultra-high field, Joint reconstruction, Low rank, Simultaneous multi slice

¹ **1. Introduction**

² Diffusion-weighted magnetic resonance imaging (DW-MRI) ([Le Bihan et al., 1986; Merboldt et al., 1985](#)) is a non-invasive modality that is sensi-
³ tive to the intravoxel Brownian motion of water molecules. DW-MRI forms
⁴ the basis for diffusion tensor imaging (DTI) ([Basser et al., 1994; Mori et al., 1999](#)) and high angular resolution diffusion imaging (HARDI) ([Tuch et al., 2002](#)), and has been widely used in acute brain ischemia diagnosis, in tumor
⁵ detection and staging, and in neuroscience ([Jones, 2010](#)).

⁶ For DW-MRI acquisition, the commonly used pulse sequence is single-
⁷ shot echo-planar imaging (SS-EPI) ([Mansfield, 1977](#)). SS-EPI is capable of
⁸ rapidly acquiring one DW image per radio-frequency excitation at the order
⁹ of 100 ms, and is thus motion robust. However, conventional SS-EPI, even
¹⁰ with three-fold accelerated acquisition ([Bammer et al., 2001](#)) using parallel
¹¹ imaging ([Roemer et al., 1990; Ra and Rim, 1993; Pruessmann et al., 1999](#);
¹² [Griswold et al., 2002](#)), still suffers from low spatial resolution and geometric
¹³ distortions.

¹⁴ In the quest for high spatial-angular-temporal-resolution and minimal-
¹⁵ geometry-distortion DW-MRI, tremendous efforts have been made. Tech-
¹⁶ niques for the correction of image distortions induced by off-resonances and
¹⁷ eddy currents have been developed ([Andersson et al., 2003](#)). Furthermore,
¹⁸ gSlider ([Setsompop et al., 2018](#)) with blipped-CAIPI ([Setsompop et al., 2012](#))
¹⁹ for simultaneous multi-slice (SMS) ([Maudsley, 1980; Breuer et al., 2005](#))
²⁰ was proposed to achieve high-resolution DW-MRI. Advanced pulse sequences
²¹ based on multi-shot EPI have also been developed, including but not limited
²² to interleaved EPI (iEPI) ([Butts et al., 1993](#)), PROPELLER ([Pipe et al., 2004](#)),

²⁶ 2002), and readout-segmented EPI (rsEPI) (Porter and Heidemann, 2009;
²⁷ Heidemann et al., 2010).

²⁸ Based on four-shot iEPI, multiplexed sensitivity encoding (MUSE) image
²⁹ reconstruction achieved DW-MRI with a sub-millimeter in-plane resolution
³⁰ and maximal b -value 800 s/mm^2 at 3 T (Chen et al., 2013). The four-shot
³¹ iEPI employed in MUSE acquired an in-plane fully-sampled k -space, except
³² partial Fourier. Every shot (segment), corresponding to four-fold under-
³³ sampling, was then reconstructed via parallel imaging to obtain shot-to-shot
³⁴ phase variation. This indicates that increasing the number of shots in MUSE
³⁵ will result in higher undersampling per shot, and consequently, degrade shot
³⁶ phase estimation (Wu and Miller, 2017).

³⁷ Alternatively, navigator-based iEPI acquisition has been proposed (Jeong
³⁸ et al., 2013; Dai et al., 2017, 2018). These proposals allow for a larger num-
³⁹ ber of shots, and hence higher spatial resolution. However, due to the use of
⁴⁰ different ESP between the imaging echo and the navigator echo, these pro-
⁴¹ posals suffered from geometric distortion mismatch between the two echoes
⁴² and thus required specific compensation methods. In contrast, rsEPI (Porter
⁴³ and Heidemann, 2009; Heidemann et al., 2010) used the same readout seg-
⁴⁴ ment for both echoes, and thus required no distortion correction of navigator
⁴⁵ echoes.

⁴⁶ Beyond the MUSE-type parallel imaging reconstruction, compressed sens-
⁴⁷ ing (Lustig et al., 2007; Block et al., 2007) has been explored. For instance,
⁴⁸ multi-shot reconstruction techniques based on structured low-rank matrix
⁴⁹ completion (MUSSELS) (Mani et al., 2017; Bilgic et al., 2019) achieved 5-
⁵⁰ shot DW-MRI with 9-fold undersampling per shot. Recently, JULEP (Dai

51 et al., 2023) incorporated explicit phase mapping into MUSSELS. These re-
52 construction techniques, i.e., MUSE, MUSSELS and JULEP, targeted the
53 reconstruction of one DW image from interleaved EPI acquisition, and did
54 not explore joint- k - q -space undersampling or reconstruction.

55 Joint- k - q -space undersampling can be achieved via proper regularization
56 along the diffusion encoding direction. Relevant examples are diffusion un-
57 dersampling with Gaussian process estimated reconstruction (DAGER) (Wu
58 et al., 2019) and magnitude-based spatial-angular locally low-rank regular-
59 ization (SPA-LLR) (Hu et al., 2020). However, DAGER addressed the re-
60 construction problem of single-shot EPI acquisition and SPA-LLR focused
61 on the reconstruction of single-band and fully-sampled iEPI acquisition.

62 In this work, we propose a Joint k - q -slice rEconsTruction framework
63 for Shift-encoded NAVigator-based interleaved EPI at 7 T (dubbed JETS-
64 NAViEPI). Our pulse sequence, NAViEPI, differs from most existing tech-
65 niques. First, NAViEPI builds upon interleaved EPI, thereby allowing for
66 fast and efficient k -space coverage. Second, inspired by rsEPI, NAViEPI en-
67 sures the same effective ESP between the imaging and the navigator echo,
68 thereby minimizing geometric distortion and allowing for the use of a larger
69 number of shots. NAViEPI essentially integrates the advantages of both iEPI
70 and rsEPI. Third, NAViEPI utilizes undersampled multi-shot iEPI, thereby
71 alleviating the SAR problem at 7 T. Fourth, NAViEPI shifts the k -space in-
72 plane sampling pattern along the phase encoding (k_y) direction. This shifting
73 creates complementary k - q -space sampling, which leads to the possibility of
74 our joint k - q -slice reconstruction. Specifically, we employ spatial-diffusion
75 overlapping LLR regularization to jointly reconstruct all diffusion encodings

⁷⁶ and multi-band slices. In vivo experiments at 7 T and comparisons with other
⁷⁷ techniques demonstrate the efficiency of our proposed method in achieving
⁷⁸ high spatial resolution DW-MRI at ultra-high field.

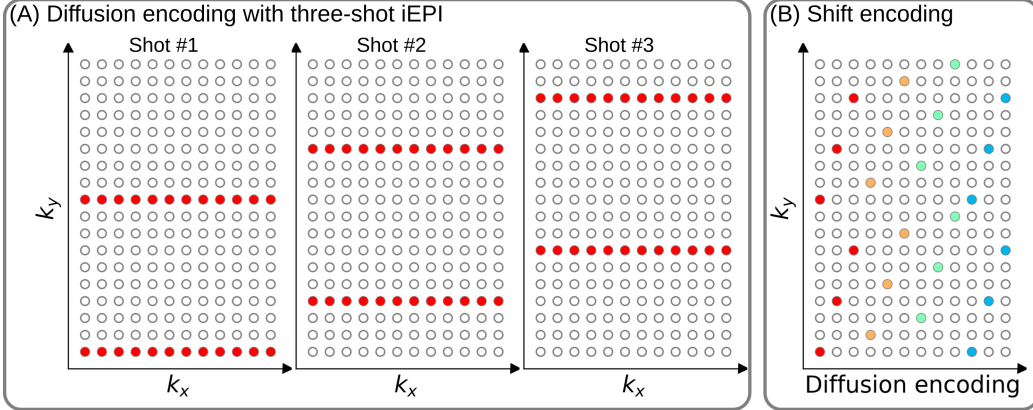


Figure 1: (A) An example DW-MRI acquisition with three-shot interleaved EPI acquisition. (B) The proposed k_y shifted diffusion encoding scheme. This example employs three shots per DW image. Therefore, every three columns have the same color.

79 2. Materials and methods

80 2.1. Multi-band shift-encoded iEPI acquisition

81 Fig. 1 (A) displays the diffusion-weighted image acquisition based on
 82 three-shot interleaved EPI with three-fold in-plane undersampling. Conven-
 83 tionally, such a sampling pattern is repeated for all diffusion directions. In
 84 contrast, we propose the k_y -shifted diffusion encoding, as shown in Fig. 1 (B).
 85 The interleaved EPI sampling pattern is shifted by one k_y line per diffusion
 86 direction, with the cycling period being the in-plane undersampling factor.

87 It is worth noting that, as shown in Fig. 1 (A), the undersampling factor
 88 of one segment is $R_{\text{in-plane}} \times N_{\text{shot}}$ (ignore multi-band undersampling here),
 89 yielding nine-fold in-plane undersampling in this example. In other words,
 90 the undersampling factor per segment linearly scales up with the number
 91 of shots. Consequently, conventional self-gating reconstruction techniques,
 92 e.g. MUSE, suffer from degraded shot-to-shot phase estimation, which in

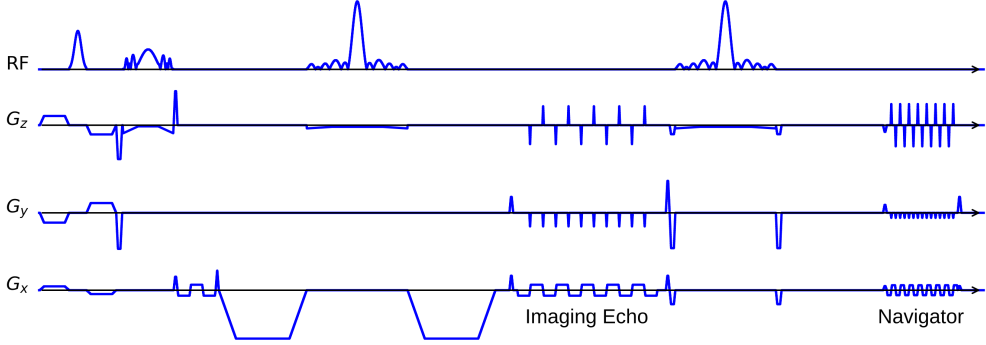


Figure 2: The NAViEPI sequence diagram. SMS is utilized for the acquisition of both imaging and navigator echoes. While the acceleration factor per navigator is the same as listed in Table 1, the acceleration factor per imaging echo is in addition linearly scaled by the number of shots.

93 turn limits the number of shots and spatial resolution.

94 *2.2. NAViEPI: Navigator-based iEPI with consistent effective ESP between
95 the imaging and the navigator echo - where iEPI meets rsEPI*

96 Instead of the self-gated MUSE with in-plane fully-sampled iEPI and
97 a limited number of shots, We propose NAVigator-based interleaved EPI
98 (NAViEPI), as illustrated in Fig. 2. Inspired by rsEPI (Porter and Hei-
99 demann, 2009), NAViEPI enforces a consistent effective ESP between the
100 imaging and the navigator echo, thereby minimizing distortion mismatch
101 between the two echoes.

102 Since one imaging echo presents one segment in multi-shot EPI acquisi-
103 tion, its effective ESP is defined as

$$\text{ESP}_{\text{eff}} = \frac{\text{ESP}}{R_{\text{in-plane}} \times N_{\text{shot}}} \quad (1)$$

104 Here, a larger number of shots (segments) increases the undersampling factor
105 per segment (see Fig. 1), but decreases the effective ESP. Since the navigator

106 echo is acquired for each segment, its in-plane undersampling factor equals
107 $R_{\text{in-plane}}$. Therefore, the effective ESP of the navigator echo must match that
108 of the imaging echo, as given in Eq. (1). With a matching effective ESP, the
109 base resolution of the navigator echo can then be determined.

110 *2.3. In vivo acquisition protocols*

111 We implemented multiple in-vivo acquisition protocols at a clinical 7 T
112 MR system (MAGNETOM Terra, Siemens Healthineers, Erlangen, Ger-
113 many) equipped with a 32-channel head coil (Nova Medical, Wilmington,
114 MA, USA) and the XR-gradient system (maximum gradient strength 80 mT/m
115 with a peak slew rate of 200 T/m/s). To calibrate coil sensitivity maps, refer-
116 ence scans employed a gradient-echo (GRE) sequence. Spectral fat saturation
117 and mono-polar diffusion-encoding gradients were used. The phase-encoding
118 direction was selected as anterior-to-posterior.

Table 1: NAViEPI acquisition protocols

Protocol	1.0 mm isotropic		sub-millimeter	
	#1	#2	#3	#4
Diffusion mode	MDDW ⁽¹⁾		3-scan trace	
Diffusion scheme	monopolar			
Diffusion direction	20	114	3	
<i>b</i> -value (s/mm ²)	1000	3-shell ⁽²⁾	1000	
<i>b</i> ₀	0	12	1	
FOV (mm ²)	200	214	220	
In-plane resolution (mm ²)	1.0		0.5	
Slice thickness (mm)	1.0		2.0	
Slices	141	114	60	
Navigator	No	No	Yes	No
Shots	4	2	5	1
TR (ms)	7700	5200	4400	8000
TEs (ms)	67	66	58/95.1	143
ESP (ms)	1.02	0.81	1.52	1.48
Bandwidth (Hz/Pixel)	1086	1460	758	
Partial Fourier			6/8	
Acceleration ⁽³⁾	1 × 3	3 × 3	3 × 2	
TA (min) ⁽⁴⁾	10 : 42	22 : 25	1 : 38	0 : 46

⁽¹⁾ MDDW: Multi-direction diffusion weighting;

⁽²⁾ 3-shell: 20, 30, and 64 directions with *b*-values of 1000, 2000, and 3000 s/mm², respectively;

⁽³⁾ Acceleration: Both in-plane and slice undersampling can be employed, denoted as (*R*_{in-plane} × *R*_{slice});

⁽⁴⁾ TA: Total acquisition time.

120 This study was approved by the local ethics committee. Three volunteers
121 with informed consent obtained before scanning participated in this study.
122 Detailed acquisition protocols are listed in Table 1. In the spirit of repro- R989.1
123ducible research, another volunteer with informed consent was recruited for
124 the scan of all acquisition protocols, and the results were displayed in Sup-
125 plementary Information.

126 *2.3.1. 20-diffusion-direction acquisition at 1 mm isotropic resolution*

127 As listed in Table 1, Protocol #1 with four-shot iEPI and without in-
128 plane undersampling was implemented. This protocol represents the acquisi-
129 tion scheme employed in many existing multi-shot reconstruction techniques,
130 (e.g., MUSE, SPA-LLR, and JULEP). The acquired data from this protocol
131 served as ground truth. Different reconstruction methods, specifically JETS,
132 MUSE, and JULEP were compared. We compared with JULEP instead of
133 MUSSELS, because JULEP uses not only structured low-rank constraints
134 but also explicit phase mapping.

135 We then retrospectively reduced the four-shot data to only one shot per
136 diffusion encoding without and with the proposed k_y shifting to simulate
137 four-fold in-plane undersampling. JETS reconstruction was performed on
138 the fully-sampled data and the retrospectively undersampled data to validate
139 the proposed k_y -shifted acquisition.

140 *2.3.2. Three-shell acquisition at 1 mm isotropic resolution*

141 Protocol #2 in Table 1 was implemented for multi-shell diffusion tensor
142 imaging (DTI) (Basser et al., 1994). We acquired a total of 114 diffusion
143 directions, whereas b_0 measurements were interspersed every ten diffusion

₁₄₄ directions. This protocol was used to demonstrate the capability of JETS
₁₄₅ in achieving high spatial-angular-temporal resolution.

₁₄₆ *2.3.3. 3-scan trace acquisition at $0.5 \times 0.5 \times 2.0 \text{ mm}^3$ voxel size*

₁₄₇ As listed in Table 1, Protocol #3 was implemented based on NAViEPI
₁₄₈ with five shots per diffusion encoding. This protocol was compared against
₁₄₉ single-shot EPI (Protocol #4) with the same spatial resolution and acceler-
₁₅₀ ation, such as to demonstrate the sampling efficiency of NAViEPI.

₁₅₁ *2.4. Forward modeling*

₁₅₂ Our proposed acquisition method yields multi-dimensional multi-band
₁₅₃ k -space data $\mathbf{y}_{c,q,s}$, where c, q, s denotes the index of the coil sensitivity
₁₅₄ map, the diffusion encoding, and the shot, respectively. Acquisition modeling
₁₅₅ needs to consider several aspects.

₁₅₆ First, the acquired k -space data \mathbf{y} is mapped from individual shot images
₁₅₇ $\mathbf{x}_{q,s,z}$ via the forward model,

$$\begin{aligned} \mathbf{y}_{c,q,s} &= \mathbf{P}_{q,s} \boldsymbol{\Sigma} \boldsymbol{\Theta}_z \mathbf{F} \mathbf{S}_c \mathbf{x}_{q,s,z} \\ \mathbf{y} &:= \mathbf{E}_1 \mathbf{x} \end{aligned} \quad (2)$$

₁₅₈ Here, the encoding matrix \mathbf{E}_1 comprises a chain of linear operators. Every
₁₅₉ shot image \mathbf{x} is point-wise multiplied by a set of coil sensitivity maps (\mathbf{S}) and
₁₆₀ Fourier transformed (\mathbf{F}). The output is then point-wise multiplied by the
₁₆₁ multi-slice phase map ($\boldsymbol{\Theta}$) with z the slice index in simultaneously excited
₁₆₂ slices. This operator shifts individual slice along the phase-encoding direction
₁₆₃ via varying phase modulation (Breuer et al., 2005). The SMS k -space data

164 is then summed (collapsed, Σ) along the slice dimension and masked (point-
165 wise multiplied, \mathbf{P}) by the sampling pattern of each diffusion encoding and
166 shot.

167 Second, for diffusion MRI based on multi-shot EPI, multiple shots ac-
168 quired for a given diffusion encoding need to be combined as one DW image
169 ($\tilde{\mathbf{x}}$). One possibility is to perform magnitude average (Chen et al., 2013)
170 or root-sum-squares (RSS) (Mani et al., 2017) of shot images. This method
171 is robust to in-plane motion, but sub-optimal concerning SNR (Guhaniyogi
172 et al., 2016). Alternatively, shot combination can be done via shot-to-shot
173 phase variation correction (Liu et al., 2005; Chen et al., 2013). This can be
174 incorporated into our formulation as point-wise multiplication between the
175 shot-to-shot phase variation (Φ) and the DW image ($\tilde{\mathbf{x}}$),

$$\mathbf{x}_{q,s,z} = \Phi_{q,s,z} \tilde{\mathbf{x}}_{q,z} \quad (3)$$

176 Note that $\tilde{\mathbf{x}}$ can be obtained by applying the adjoint of Φ to \mathbf{x} . In MUSE,
177 Φ is obtained by parallel imaging reconstruction of all shots with subsequent
178 phase smoothing of every shot image. Based on this phase correction, the
179 complete forward model follows

$$\mathbf{y} := \mathbf{E}_2 \tilde{\mathbf{x}} = \mathbf{E}_1 \Phi \tilde{\mathbf{x}} \quad (4)$$

180 where the encoding matrix \mathbf{E}_2 comprises the chain of the shot-to-shot phase
181 variation Φ and the encoding matrix \mathbf{E}_1 . We implemented these two encoding
182 operators in SigPy (Ong and Lustig, 2019).

183 2.5. Joint k - q -slice reconstruction

184 Based on the generalized forward models in Eqs. (2) and (4), our proposed
185 joint k - q -slice reconstruction can be formulated as a three-step approach.

186 **I. Navigator echo reconstruction.** The acquisition of navigator echoes
 187 follows the forward model in Eq. (2), so the reconstruction of navigator
 188 echoes can be formulated as:

$$\operatorname{argmin}_{\mathbf{x}} \|\mathbf{y} - \mathbf{E}_1 \mathbf{x}\|_2^2 + \lambda \mathbf{R}(\mathbf{x}) \quad (5)$$

189 where $\mathbf{R}(\mathbf{x})$ denotes the regularization functional with the regularization
 190 strength λ . In this work, ℓ^2 regularization was used, i.e., $\mathbf{R}(\mathbf{x}) =$
 191 $\|\mathbf{x}\|_2^2$. In the case of self-navigating (i.e., no navigator acquired) as
 192 Protocol #2, the central k -space region (i.e., 1/4 of the full image matrix)
 193 of each segment is used as \mathbf{y} in Eq. (5).

194 **II. Iterative phase smoothing.** Shot-to-shot phase variation was ex-
 195 tracted from the reconstructed navigator echo phases. Assuming that
 196 phase images are spatially smooth (Chen et al., 2013; Dai et al., 2023),
 197 we employed the adaptive Hanning filter to smooth shot phases,

R990.12

$$\mathbf{x} = \mathbf{F}^{-1} \mathcal{H}^K \mathbf{F} \mathbf{x} \quad (6)$$

198 where x is the reconstructed navigator image from Step I. \mathcal{H} is the Han-
 199 ning window with the non-negative integer K . K controls the width of
 200 the Hanning window.

201 **III. Shot-combined reconstruction.** Joint reconstruction of all DW im-
 202 ages using the shot-combined forward model \mathbf{E}_2 with shot-to-shot phase
 203 variation from Step II reads:

$$\operatorname{argmin}_{\tilde{\mathbf{x}}} \|\mathbf{y} - \mathbf{E}_2 \tilde{\mathbf{x}}\|_2^2 + \lambda \|\mathbf{T}(\tilde{\mathbf{x}})\|_* \quad (7)$$

204 Here, LLR regularization was employed in the local spatial-diffusion
 205 matrices, based on the theory of partially separable functions (Liang,

206 2007; Trzasko and Manduca, 2011; Zhang et al., 2015). \mathbf{T} represents
207 a linear operator that firstly slides a local patch window through all
208 DW images and then flattens every set of local patches to construct
209 two-dimensional (2D) spatial-diffusion matrices. The spatial dimension
210 equals the block size, and the diffusion dimension is the number of dif-
211 fusion encodings. $\|\mathbf{T}(\tilde{\mathbf{x}})\|_*$ is the nuclear norm, i.e. the sum of singular
212 values of a spatial-diffusion matrix. This nuclear norm regularization
213 was accomplished via singular value thresholding (SVT) of each spatial-
214 diffusion matrix (Cai et al., 2010). After SVT, the adjoint of \mathbf{T} , \mathbf{T}^H ,
215 was needed to reorder pixel values from the spatial-diffusion matrices
216 back to DW images. To alleviate checkerboard artifacts induced by
217 LLR regularization with non-overlapping blocks (Hu et al., 2020), we
218 employed overlapping blocks. In this case, values from overlapping po-
219 sitions are summed up to the output of \mathbf{T}^H . To enable the correct use
220 of \mathbf{T}^H , we element-wise divided the output of \mathbf{T}^H by a scaling matrix.
221 This matrix was obtained via $\mathbf{T}^H(\mathbf{T}(\mathbf{1}))$, where $\mathbf{1}$ denotes the matrix
222 of all ones with the same shape as the input \mathbf{x} .

223 2.6. Reconstruction

224 The acquired raw data was read in by twixtools (<https://github.com/pehses/twixtools>). Ramp-sampling regridding and FOV/2-ghost correc-
225 tion were also performed in twixtools. Subsequently, coil sensitivity maps
226 were computed from reference scans using ESPIRiT (Uecker et al., 2014) in
227 SigPy (Ong and Lustig, 2019).

228 With this pre-processing as well as the implemented forward models and
229 proximal operator, the inverse problem in Eq. (7) was solved by the alter-

231 nating direction method of multipliers (ADMM) (Boyd et al., 2010).

232 ADMM solves the minimization problems in an alternating update scheme,

$$\begin{cases} \mathbf{x}^{(k+1)} := \underset{\mathbf{x}}{\operatorname{argmin}} \| \mathbf{y} - \mathbf{E}(\mathbf{x}) \|^2 + \rho/2 \| \mathbf{T}\mathbf{x} - \mathbf{z}^{(k)} + \mathbf{u}^{(k)} \|_2^2 \\ \mathbf{z}^{(k+1)} := \mathcal{T}_{\lambda/\rho}(\mathbf{T}\mathbf{x}^{(k+1)} + \mathbf{u}^{(k)}) \\ \mathbf{u}^{(k+1)} := \mathbf{u}^{(k)} + \mathbf{T}\mathbf{x}^{(k+1)} - \mathbf{z}^{(k+1)} \end{cases} \quad (8)$$

233 where k denotes the ADMM iteration. \mathbf{z} is the auxiliary variable ($\mathbf{z} = \mathbf{T}\mathbf{x}$),
234 and \mathbf{u} is the Lagrangian multipliers. Importantly, when solving Eq. (2), \mathbf{x}
235 denotes shot images and \mathbf{E} denotes \mathbf{E}_1 in Eq. (8). In contrast, \mathbf{x} denotes shot-
236 combined images and \mathbf{E} denotes \mathbf{E}_2 when solving Eq. (4). \mathbf{x} can be solved
237 using linear least square algorithms, e.g. conjugate gradients (Hestenes and
238 Stiefel, 1952), while \mathbf{z} is updated via singular value thresholding (\mathcal{T}) with
239 the thresholding parameter λ/ρ . The coupling parameter ρ is effective in
240 both the update of \mathbf{x} and \mathbf{z} . It acts as Tikhonov regularization strength
241 when updating \mathbf{x} , but also inversely scales the thresholding strength when
242 updating \mathbf{z} .

243 In this work, 15 ADMM iterations with $\rho = 0.05$ and $\lambda = 0.08$ were used.

244 All reconstructions were done on a single A100 SXM4/NVLink GPU with
245 40 GB memory (NVIDIA, Santa Clara, CA, USA).

246 We compared our proposed joint reconstruction with established multi-
247 shot reconstruction techniques, specifically, MUSE (Chen et al., 2013) and
248 JULEP (Dai et al., 2023), hosted on GitHub by Dr. Dai (Dai et al., 2023).
249 Further, we performed the local-PCA denoising (Cordero-Grande et al., 2019)
250 as implemented in MRtrix (Tournier et al., 2019) on the MUSE reconstructed
251 complex DW images.

252 The in vivo data acquired from Protocol #2 in Table 1 consisted of 126

253 diffusion directions, which exceeds the available GPU memory. Therefore,
254 the 126 data volumes were uniformly split into three parts for our JETS
255 reconstruction with a LLR block width of 6 and the LLR regularization in
256 both Steps I and III in Section 2.5. In addition, MUSE reconstruction was
257 also performed, followed by the local-PCA denoising. Reconstructed DWIs
258 were then processed by DiPy ([Garyfallidis et al., 2014](#)) to obtain color-coded
259 fractional anisotropy (cFA) maps.

260 **3. Results**

261 *3.1. Smoothing of shot-to-shot phase variation*

262 Navigators were acquired with the acceleration rate as listed in Table 1.

263 Besides, the base resolution of navigators (e.g. 32 in Protocol #3 in Table 1)

264 was smaller than imaging echoes. As a result, reconstructed navigator phases

265 (refer to the first column in Fig. 3) from Step I in Section 2.5 are not spatially

266 smooth. Such phases, when used in the shot-combined reconstruction, result

267 in signal void artifacts in DW images. To address this problem, we utilized

268 the phase smoothing procedure. As shown in Fig. 3, the ripple-like phase ar-

R990.12

269 tifact disappears at $K = 5$, while retaining the shot-to-shot phase variation.

270 In contrast, a larger K (e.g., $K = 20$) makes the filter too strong and even

271 partially removes phase variation.

272 *3.2. Comparison to MUSE and JULEP with four-shot iEPI acquisition*

273 The iterative phase smoothing was also applicable to MUSE-type self-

274 navigating reconstruction, where shot phases were reconstructed from imag-

275 ing echoes. Fig. 4 compares our proposed JETS with MUSE (Chen et al.,

276 2013), MUSE with complex-valued local-PCA denoiser (Cordero-Grande et al.,

277 2019), and JULEP (Dai et al., 2023). The residual noise from MUSE can be

278 largely removed by the denoiser. However, when compared to JETS, the de-

279 noiser shows residual noise patterns within the globus pallidus (indicated by

280 the red arrow). JETS also shows better denoising than JULEP. The reason

281 is that JETS enforces spatial-diffusion regularization, whereas JULEP for-

282 mulates structured low-rank regularization of the four shots for one diffusion

283 encoding.

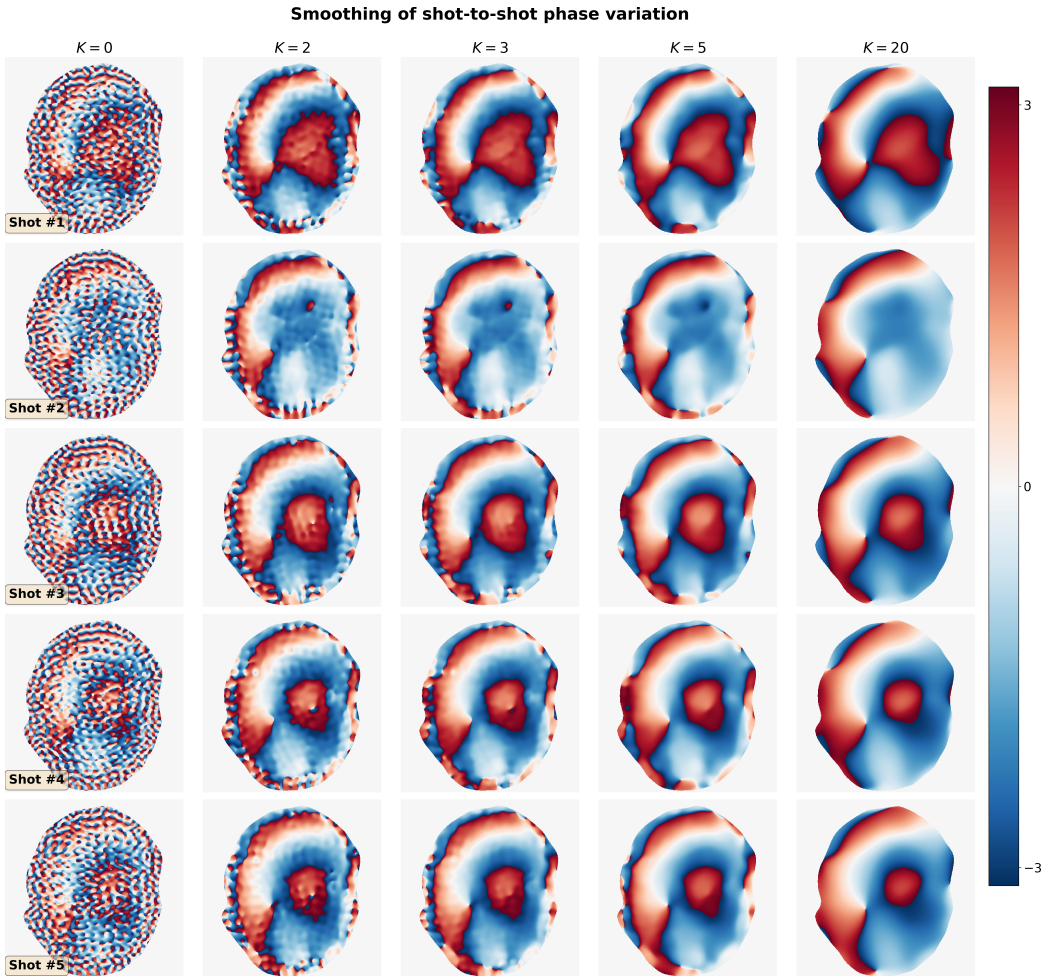


Figure 3: Smoothing of shot-to-shot phase variation according to Eq. (6). Navigators from Protocol #3 were reconstructed based on Step I in Section 2.5 and then used as the input (the column with $K = 0$).

8th DW image from 4-shot iEPI @ 1 mm ISO

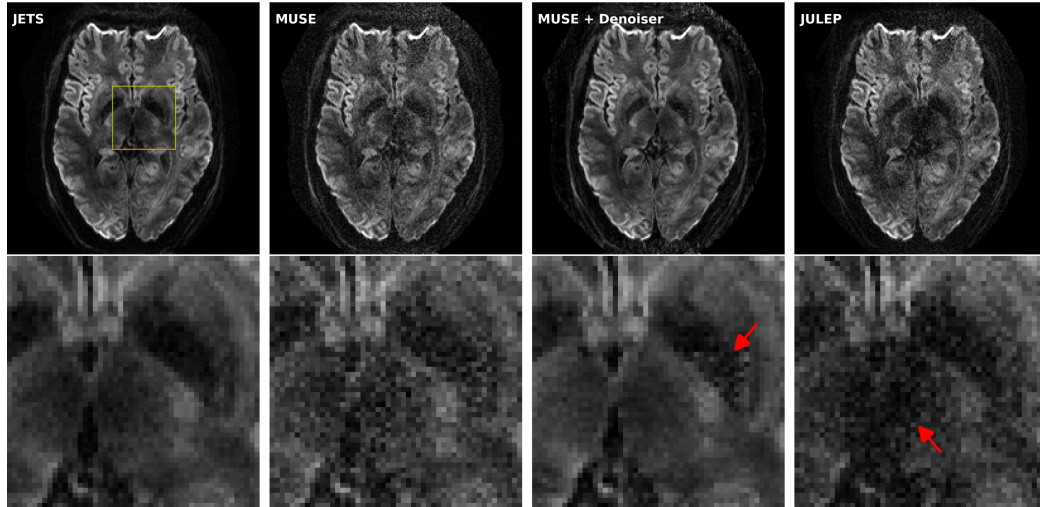


Figure 4: Reconstructed DW images (the 8th diffusion encoding) based on 4-shot iEPI acquisition with 1 mm isotropic resolution (Protocol #1 in Table 1). Four reconstruction methods are compared (from left to right): JETS, MUSE, MUSE with denoiser, and JULEP. The 2nd row displays the magnified views of the yellow square. The image from the denoiser (3rd column) shows residual noise patterns within the globus pallidus (indicated by the red arrow). The JULEP reconstruction (4th column) shows signal dropout in the central region (indicated by the red arrow).

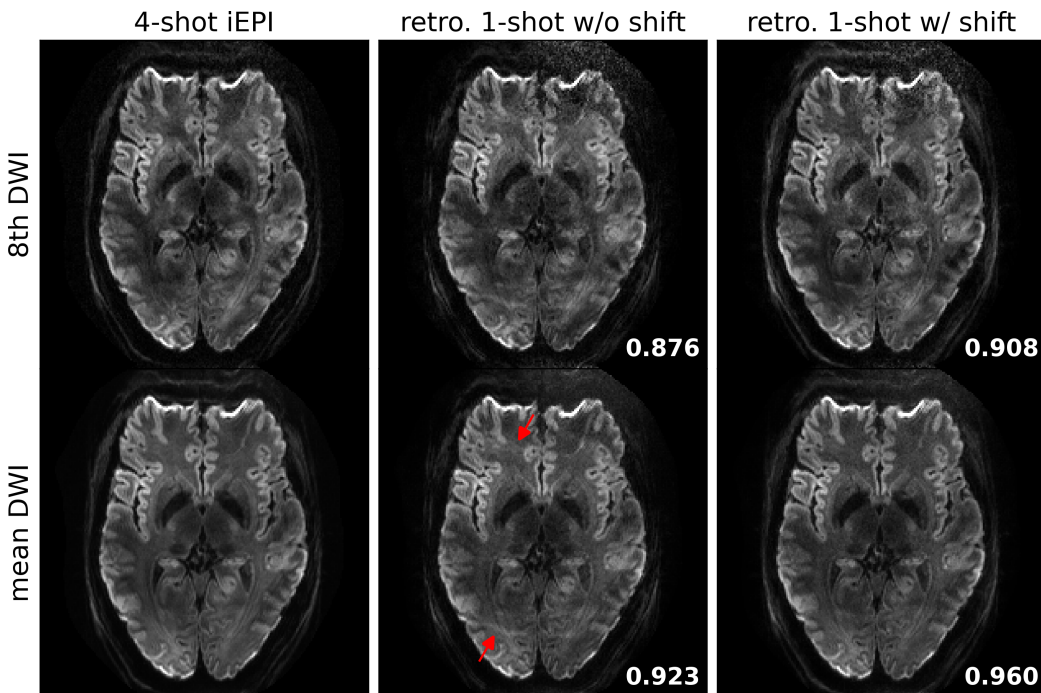


Figure 5: Quantitative validation of the proposed k_y -shift encoding sampling pattern based on 4-shot iEPI acquisition with 1 mm isotropic resolution (Protocol #1 in Table 1). (Top) the 8th diffusion encoding and (bottom) mean DWI over 20 diffusion encodings. (1st column) JETS reconstruction of 4-shot iEPI acquisition is used as the ground truth. The 2nd and the 3rd column displays JETS reconstruction of retrospectively undersampled 1-shot acquisition without and with k_y shifting, respectively. Residual aliasing artifacts are visible in the reconstruction without k_y shifting, as indicated by the red arrows. Structural similarity (SSIM) values are computed and displayed in the bottom right corners.

284 3.3. Retrospectively undersampling from the four-shot iEPI acquisition

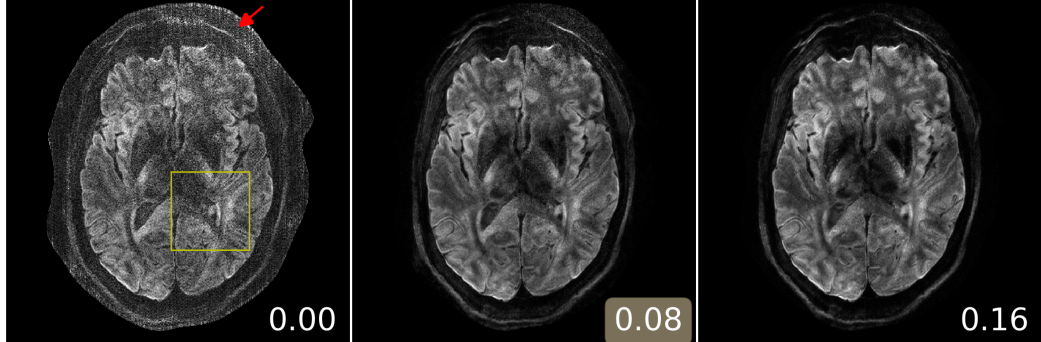
285 JETS reconstruction results on the four-shot prospectively fully-sampled
286 data from Protocol #1 in Table 1, as well as on the retrospectively under-
287 sampled one-shot data without and with the proposed k_y shift are displayed
288 in Fig. 5. Residual aliasing artifacts are visible in the reconstruction with-
289 out k_y shifting, as indicated by the red arrows. In contrast, the k_y shifting
290 scheme supplies a complementary k - q -space sampling pattern, which is bene-
291 ficial for joint reconstructions such as JETS. As shown in Fig. 5, JETS results
292 in improved SSIM values and reduced aliasing artifacts, when compared to
293 the reconstruction without k_y shifting. Figs. 4 and 5 show a slice containing R990.7
294 the globus pallidus with strong T_2 -weighted contrast and highlighting the
295 advantage of k_y -shift encoding in reducing undersampling artifacts.

296 3.4. Analysis of reconstruction parameters

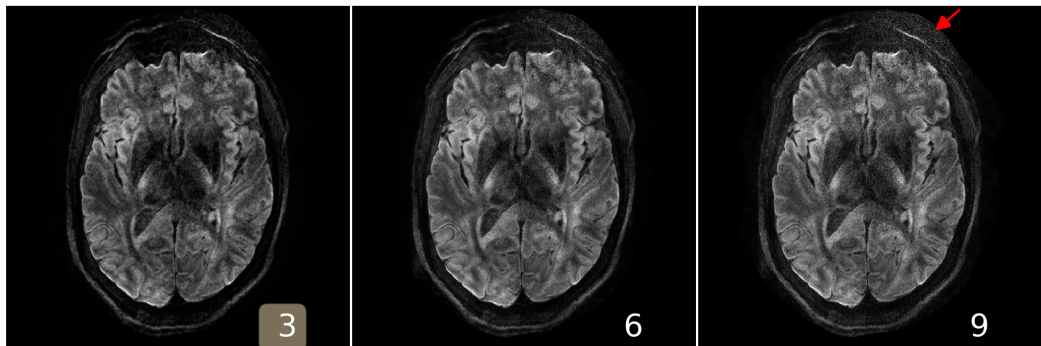
297 Here we provide a systematic analysis of the proposed JETS reconstruc-
298 tion with LLR regularization applied to the spatial-diffusion dimension, as
299 shown in Fig. 6.

300 First, we varied the regularization strength λ . We tested values of 0, 0.08,
301 and 0.16. The reconstruction with $\lambda = 0$ in Eq. (7) corresponds to parallel
302 imaging reconstruction without LLR regularization. It is worth noting that
303 the proposed NAViEPI sequence demonstrates high-quality sub-millimeter
304 DW images ($0.5 \times 0.5 \times 2.0 \text{ mm}^3$ in this example). The DW images can be
305 further improved with the use of LLR regularization, i.e., reduced noise, as
306 seen in the reconstruction with $\lambda = 0.08$. Increasing λ (e.g. 0.16) further
307 reduces noise, but at the cost of increased blurring. Therefore, $\lambda = 0.08$ was
308 selected in this work.

(A) varying λ , keeping block as 6 and stride as 1



(B) varying block width, keeping λ 0.08 and stride 1



(C) varying stride, keeping λ as 0.08 and block as 6

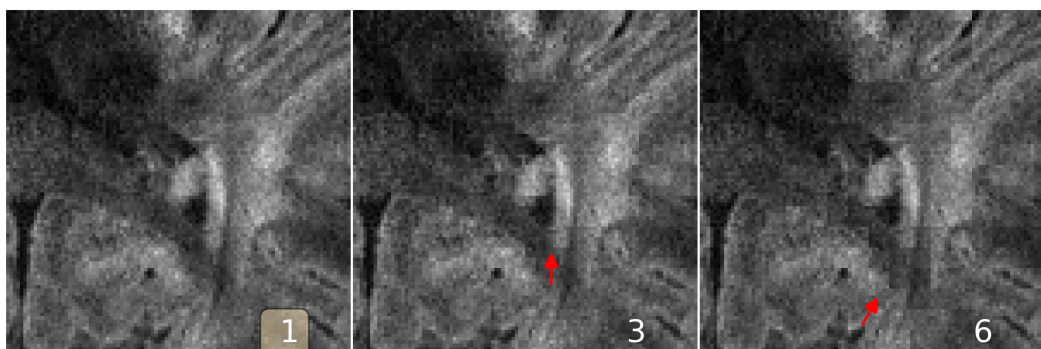


Figure 6: Analysis of reconstruction parameters based on the 3-scan trace acquisition with $0.5 \times 0.5 \times 2.0 \text{ mm}^3$ (Protocol #3 in Table 1). Displayed are JETS reconstructed single-direction DW images. (A) Varying the regularization strength λ from 0 to 0.08 and 0.16. (B) Varying the block width from 3 to 6 and 9. The red arrow indicates increased noise with the large block width. (C) Varying the stride size from 1 to 3 (partially overlapping) and 6 (non-overlapping). The red arrows indicate blocky artifacts.

309 Second, besides the regularization strength, the block size (i.e., the area
310 of 2D patches) also plays a role in denoising. We employed square blocks in R990.4.a
311 this work. Here, **the block width** of 3 shows the best denoising as compared
312 to 6 and 9, especially in the peripheral brain region.

313 Third, we varied the stride, i.e., the step from one local patch to the
314 next. The use of overlapping LLR (Fig. 6 (C) left) better suppresses blocky
315 artifacts, compared to **the partially overlapping (stride < block)** LLR (Fig. 6
316 (C) middle) and **the non-overlapping (stride = block)** LLR (Fig. 6 (C) right). R990.4.b

317 *3.5. Sampling efficiency of NAViEPI*

318 As shown in Fig. 7, NAViEPI achieves sub-millimeter resolution (voxel
319 size $0.5 \times 0.5 \times 2.0 \text{ mm}^3$) with the use of a 5-shot acquisition. When compared
320 to a single-shot acquisition with the same voxel size, the acquisition time of
321 NAViEPI is about two times longer, but the image quality of NAViEPI is
322 remarkably improved.

323 In the sub-millimeter imaging scenario, the increased base resolution re-
324 quires longer TE (143 ms) in the single-shot acquisition, which results in
325 significant signal loss due to T_2 relaxation. Therefore, sub-millimeter DWI
326 necessitates multi-shot acquisition, which is subject to shot-to-shot phase
327 variation and long scan time. However, NAViEPI solves both challenges. The
328 5-shot acquisition reduces TE to 58 ms, and thus retains SNR significantly
329 compared to the single-shot acquisition. Moreover, the JETS reconstruction
330 can help to reduce noise and improve structural visibility.

331 Fig. 8 shows the JETS reconstructed b_0 and TRACE images in different
332 slice locations. Admittedly, the lower brain region (e.g. slice #22) exhibits in-
333 homogeneous and lower signal intensity than the upper slices. Such inhomogeneity

3-scan trace acquisition with voxel size $0.5 \times 0.5 \times 2.0 \text{ mm}^3$

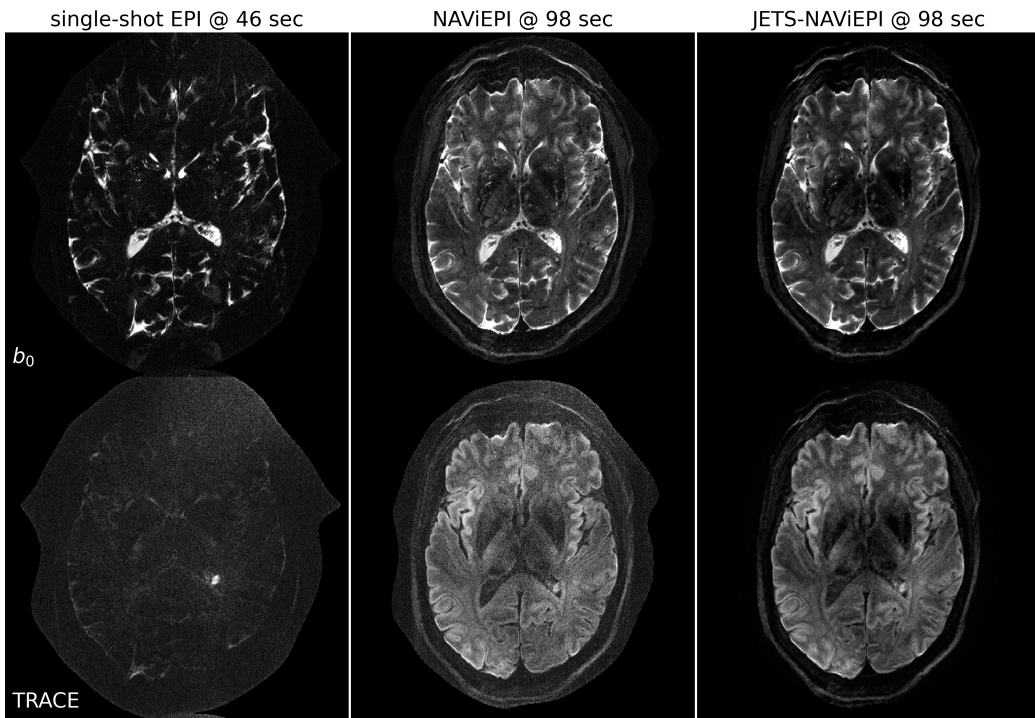


Figure 7: Sampling efficiency of the proposed NAViEPI sequence. 5-shot NAViEPI acquisition with the voxel size $0.5 \times 0.5 \times 2.0 \text{ mm}^3$ (Protocol #3) was compared with single-shot EPI acquisition (Protocol #4). Both the 1st and the 2nd columns were reconstructed via parallel imaging without LLR regularization, whereas the 3rd column was reconstructed via JETS.

3-scan trace acquisition with voxel size $0.5 \times 0.5 \times 2.0 \text{ mm}^3$

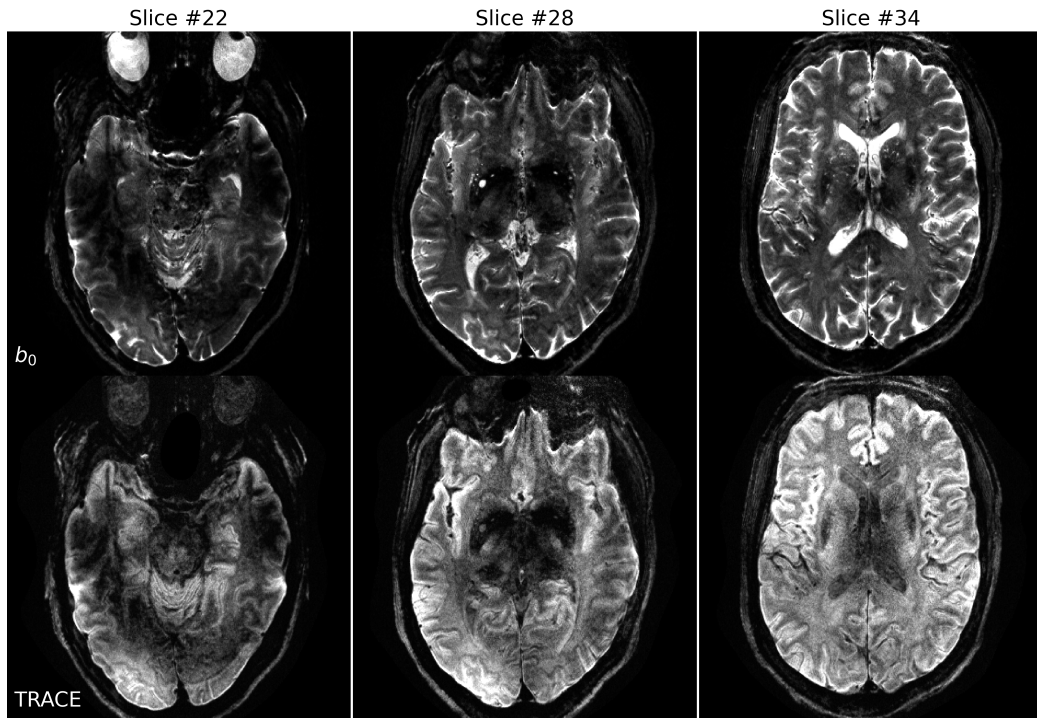


Figure 8: Reconstruction of the 3-scan trace acquisition with the voxel size $0.5 \times 0.5 \times 2.0 \text{ mm}^3$ (Protocol #3) at different slices.

334 geneity can be alleviated with the use of multi-channel parallel transmission
335 (Katscher et al., 2003; Grissom et al., 2010).

336 Here, Figs. 6 and 7 select a slice with a benign lesion (the circular bright R990.7
337 spot) within the left ventricle. Fig. 8 displays three representative slices: (left)
338 the lower brain region which identifies the B_1^+ field inhomogeneity, (middle)
339 the middle brain slice which shows susceptibility artifacts in the frontal re-
340 gion, and (right) the upper brain slice which shows the ventricle.

341 *3.6. Diffusion tensor imaging*

342 Protocol #2 in Table 1 yields an acceleration factor of 6×3 per shot, re-
343 sulting in severe noise amplification in MUSE reconstructed DWIs, as shown
344 in Fig. 9. Here, a slice that highlights the corpus callosum is displayed, and R990.7
345 the diffusion direction at the b -value of 3000 s/mm^2 with bright signal within
346 the corpus callosum is shown. The local-PCA denoiser substantially removes
347 noise, but the DWI at high b -values still illustrates more noise, compared to
348 the proposed JETS reconstruction. On the other hand, we applied the lo-
349 cal-PCA denoiser before the shot combination in MUSE. As shown in Fig. 9, R990.3.b.1
350 this approach is less effective compared to the application of the denoiser
351 after the shot combination, because shot images were reconstructed from the
352 central k -space region and have a coarse resolution.

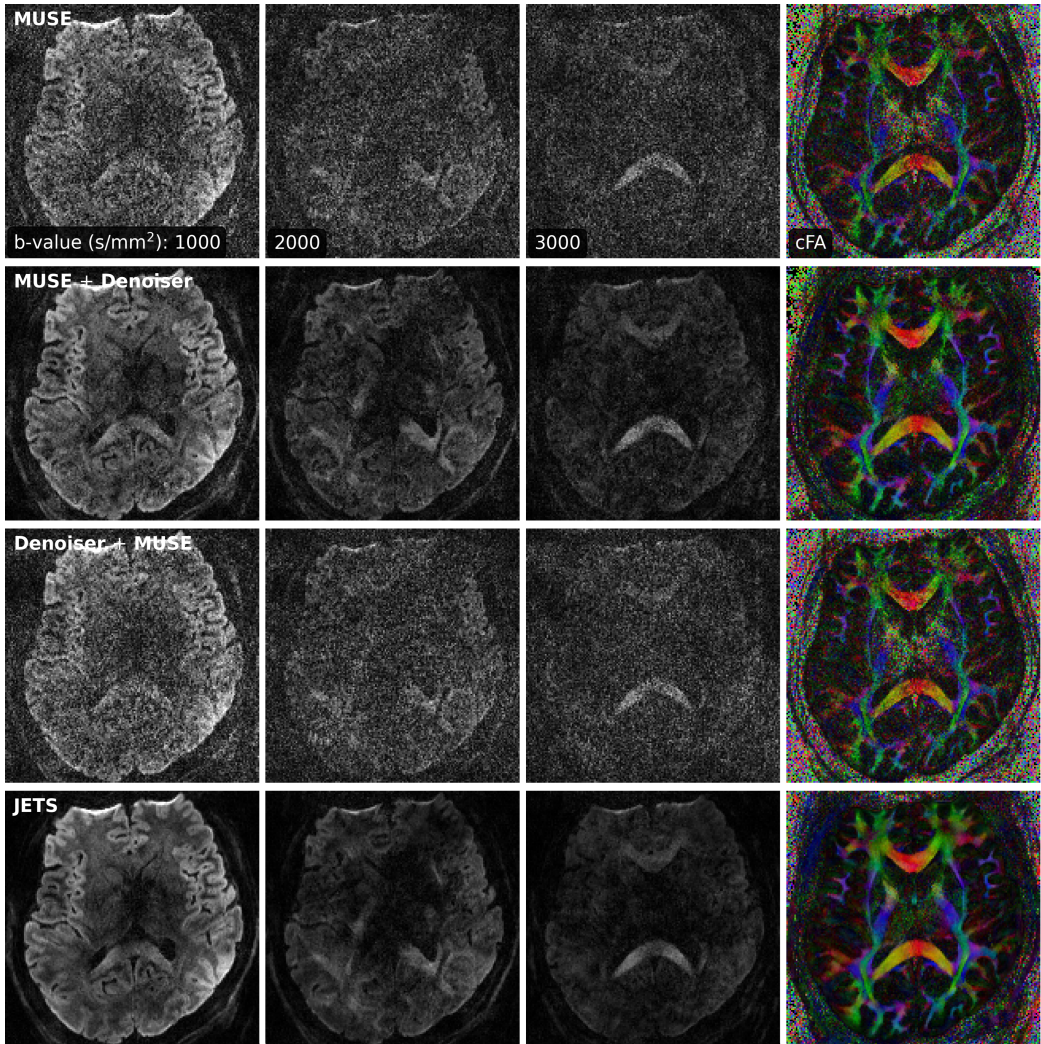


Figure 9: Comparison of three-shell DWIs and cFA maps with data acquired by Protocol #2 in Table 1. Reconstruction methods from top to bottom were MUSE, MUSE with the local-PCA denoiser, the application of the denoiser on shot images before the shot combination in MUSE, and the proposed JETS method.

353 **4. Discussion**

354 This work reports a novel DW-MRI technique, JETS-NAViEPI. NAViEPI
355 (1) achieves the fast and efficient acquisition of both imaging and navigator
356 echoes, (2) enforces consistent effective ESP between the two echoes, and (3)
357 allows for undersampled iEPI as well as a large number of shots. Moreover,
358 compared to the single-shot acquisition, joint k - q -slice reconstruction with k_y -
359 shift encoding on NAViEPI retains SNR and reduces aliasing artifacts in DW
360 images. As a result, JETS-NAViEPI renders high spatiotemporal resolution
361 diffusion MRI protocols in 7 T, e.g., a 3-scan trace acquisition with the voxel
362 size $0.5 \times 0.5 \times 2.0 \text{ mm}^3$ at 1.5 min.

363 One limitation of JETS-NAViEPI is the long reconstruction time due to
364 the simultaneous reconstruction of all DW images and the use of overlapping
365 locally low-rank regularization. The reconstruction for the Protocol #3 in
366 Table 1 on an A100 GPU takes about 2 min per multi-band slice. To reduce
367 the computation time, coil compression algorithms (Buehrer et al., 2007;
368 Huang et al., 2008) can be employed to reduce the number of coils for image
369 reconstruction. Moreover, one can deploy multi-GPU distributed computing
370 or modern optimization algorithms (e.g. stochastic gradient descent) (Ong
371 et al., 2020) to speed up the reconstruction.

372 Neither the signal modeling in Eqs. (2) and (4) nor the LLR regularization
373 considers the subject motion. In the presence of motion, the regularized
374 reconstruction can degrade. To overcome this problem, scout-informed mo-
375 tion estimation and reconstruction (Polak et al., 2022) could be integrated
376 into the framework.

377 Another potential extension of this work is to incorporate distortion cor-

378 rection. The standard distortion correction method is known as TOPUP
379 (Andersson et al., 2003), which acquires two scans with opposing phase-
380 encoding directions to obtain the field inhomogeneity map and then per-
381 forms conjugate phase reconstruction to correct for distortion. Alternatively, R989.4,
382 a multi-echo acquisition could be used for the coil sensitivity reference scan, R990.13
383 such that both coil sensitivity and B_0 field inhomogeneity maps could be
384 reconstructed from the data.

385 This work employed a single regularization weight λ to enforce low rank-
386 ness along the spatial-diffusion direction. However, SNR may be heteroge-
387 neous within the FOV. Therefore, one single regularization scalar may be
388 inadequate to cover the whole FOV. Beyond this SVT-based reconstruction,
389 one can seek to use machine learning to learn a q -space prior as the regularizer
390 (Hammernik et al., 2018; Lam et al., 2019; Mani et al., 2021).

391 Although NAViEPI employs navigators for the acquisition of shot-to-
392 shot phase variation, it is worth noting that phase behavior depends on
393 several hard-to-control factors such as pulsatile motion, bulk motion, loca-
394 tions within the brain, and diffusion sensitization strength. Therefore, more
395 comprehensive modeling or post-processing such as image registration can
396 be considered in future work.

397 This work compared LLR regularized JETS to MUSE post-processed by
398 the local PCA denoiser (Cordero-Grande et al., 2019). Both the LLR reg-
399 ularization and the local PCA denoiser are based on the principle that low
400 rankness exists in the spatial-diffusion dimension, where the spatial content
401 is extracted from local patches within the full image volume and the diffusion
402 dimension is from the q -space encoding. Both of them demonstrate effective
R990.3.b.2

403 denoising capabilities and allow for high-quality DW-MRI image reconstruc-
404 tion from the accelerated acquisition.

405 Technically, the LLR regularization is realized by soft thresholding of
406 the singular values of the spatial-diffusion matrices, whereas the denoiser
407 performs hard thresholding. Both approaches demonstrate effective noise
408 removal. In the scenario of accelerated acquisitions, one can employ both
409 approaches to maximally boost SNR, i.e., the use of LLR regularization for
410 image reconstruction followed by the denoiser as a post-processing step.

411 While this work reconstructs all DW images and then performs model
412 fitting, an alternative approach is to directly estimate b_0 and diffusion ten-
413 sors from measured k - q -space data using model-based reconstruction (Knoll
414 et al., 2015; Dong et al., 2018; Shafieizargar et al., 2023). Compared to DW
415 image reconstruction, model-based reconstruction solves for a fewer number
416 of unknowns, but requires strict diffusion tensor modeling and the use of
417 nonlinear least square solvers.

418 **5. Conclusions**

419 We demonstrated the JETS-NAViEPI technique, which integrates a k_y -
420 shifted encoding navigator-based interleaved EPI sequence and joint recon-
421 struction with overlapping locally low-rank regularization for high spatial-
422 angular-temporal resolution DW-MRI at 7 T. This technique allows for high-
423 quality DW image reconstruction with accelerated acquisitions.

424 **Funding**

425 Funding by the German Research Foundation (DFG) is gratefully ac-
426 knowledged (projects 513220538, 512819079; and project 500888779 of the
427 RU5534 MR biosignatures at UHF). In addition, funding by the National
428 Institutes of Health (NIH), R01 EB024532 and P41 EB017183, is gratefully
429 acknowledged.

430 In addition, we gratefully acknowledge the scientific support and HPC
431 resources provided by the Erlangen National High Performance Computing
432 Center (NHR@FAU) of Friedrich-Alexander-University Erlangen-Nuremberg
433 (FAU) under the NHR project b143dc. NHR funding is provided by federal
434 and Bavarian state authorities. NHR@FAU hardware is partially funded by
435 the German Research Foundation (DFG) – 440719683.

436 **Data and code available statement**

437 In the spirit of reproducible and open science, we publish our source
438 code (<https://github.com/ZhengguoTan/sigpy>) as well as the raw k -space
439 data (<https://doi.org/10.5281/zenodo.7548595>). We also provide inter-
440 active demonstrations of the reconstruction procedure (https://github.com/ZhengguoTan/demo_jets_diffusion_mri_7t).

442 **Acknowledgments**

443 The authors thank Dr. Peter Neher for the discussion on MITK-Diffusion.
444 The authors thank Dr. Berkin Bilgic for making the MUSSELS source code
445 (<https://bit.ly/2QgBg9U>) publically available, Dr. Erpeng Dai for sharing
446 the JULEP source code (<https://github.com/daiexp/JULEP>) on GitHub,

447 and Dr. Zhiyong Zhang for sharing the SPA-LLR source code (<https://github.com/ZZgroupSJTU/PMCmsDTI>) on GitHub. The authors also thank
448
449 Dr. Philipp Ehses for the discussion on twixtools (<https://github.com/pehses/twixtools>).
450

451 **References**

- 452 Andersson, J.L.R., Skare, S., Ashburner, J., 2003. How to correct suscepti-
453 bility distortions in spin-echo echo-planar images: application to diffusion
454 tensor imaging. NeuroImage 20, 870–888. doi:[10.1016/S1053-8119\(03\)00336-7](https://doi.org/10.1016/S1053-8119(03)00336-7).
455
- 456 Bammer, R., Keeling, S.L., Augustin, M., Pruessmann, K.P., Wolf, R., Stoll-
457 berger, R., Hartung, H.P., Fazekas, F., 2001. Improved diffusion-weighted
458 single-shot echo-planar imaging (EPI) in stroke using sensitivity encoding
459 (SENSE). Magn. Reson. Med. 46, 548–554. doi:[10.1002/mrm.1226](https://doi.org/10.1002/mrm.1226).
- 460 Basser, P.J., Mattiello, J., Le Bihan, D., 1994. MR diffusion tensor
461 spectroscopy and imaging. Biophys. J. 66, 259–267. doi:[10.1016/S0006-3495\(94\)80775-1](https://doi.org/10.1016/S0006-3495(94)80775-1).
462
- 463 Bilgic, B., Chatnuntawech, I., Manhard, M.K., Tian, Q., Liao, C., Iyer, S.S.,
464 Cauley, S.F., Huang, S.Y., Polimeni, J.R., Wald, L.L., Setsompop, K.,
465 2019. Highly accelerated multishot echo planar imaging through synergistic
466 machine learning and joint reconstruction. Magn. Reson. Med. 82, 1343–
467 1358. doi:[10.1002/mrm.27813](https://doi.org/10.1002/mrm.27813).
- 468 Block, K.T., Uecker, M., Frahm, J., 2007. Undersampled radial MRI with

- 469 multiple coils. Iterative image reconstruction using a total variation con-
470 straint. Magn. Reson. Med. 57, 1186–1098. doi:[10.1002/mrm.21236](https://doi.org/10.1002/mrm.21236).
- 471 Boyd, S., Parikh, N., Chu, E., Peleato, B., Eckstein, J., 2010. Distributed
472 optimization and statistical learning via the alternating direction method
473 of multipliers. Foundations and Trends in Machine Learning 3, 1–122.
474 doi:[10.1561/2200000016](https://doi.org/10.1561/2200000016).
- 475 Breuer, F.A., Blaimer, M., Heidemann, R.M., Mueller, M.F., Griswold, M.A.,
476 Jakob, P.M., 2005. Controlled aliasing in parallel imaging results in higher
477 acceleration (CAPIRINHA) for multi-slice imaging. Magn. Reson. Med.
478 53, 684–691. doi:[10.1002/mrm.20401](https://doi.org/10.1002/mrm.20401).
- 479 Buehrer, M., Pruessmann, K.P., Boesiger, P., Kozerke, S., 2007. Array com-
480 pression for MRI with large coil arrays. Magn. Reson. Med 57, 1131–1139.
481 doi:[10.1002/mrm.21237](https://doi.org/10.1002/mrm.21237).
- 482 Butts, K., Riederer, S.J., Ehman, R.L., Thompson, R.M., Jack, C.R., 1993.
483 Interleaved echo planar imaging on a standard MRI system. Magn. Reson.
484 Med. 31, 67–72. doi:[10.1002/mrm.1910310111](https://doi.org/10.1002/mrm.1910310111).
- 485 Cai, J.F., Candès, E.J., Shen, Z., 2010. A singular value threshold-
486 ing algorithm for matrix completion. SIAM. J. Optim. 20, 1956–1982.
487 doi:[10.1137/080738970](https://doi.org/10.1137/080738970).
- 488 Chen, N.K., Guidon, A., Chang, H.C., Song, A.W., 2013. A robust multi-
489 shot scan strategy for high-resolution diffusion weighted MRI enabled by
490 multiplexed sensitivity-encoding (MUSE). NeuroImage 72, 41–47. doi:[10.1016/j.neuroimage.2013.01.038](https://doi.org/10.1016/j.neuroimage.2013.01.038).

- 492 Cordero-Grande, L., Christiaens, D., Hutter, J., Price, A.N., Hajnal, J.V.,
493 2019. Complex diffusion-weighted image estimation via matrix recovery
494 under general noise models. NeuroImage 200, 391–404. doi:[10.1016/j.neuroimage.2019.06.039](https://doi.org/10.1016/j.neuroimage.2019.06.039).
- 495
- 496 Dai, E., Ma, X., Zhang, Z., Yuan, C., Guo, H., 2017. Simultaneous multislice
497 accelerated interleaved EPI DWI using generalized blipped-CAIPI acqui-
498 sition and 3D K-space reconstruction. Magn. Reson. Med. 77, 1593–1605.
499 doi:[10.1002/mrm.26249](https://doi.org/10.1002/mrm.26249).
- 500 Dai, E., Mani, M., McNab, J.A., 2023. Multi-band multi-shot diffu-
501 sion MRI reconstruction with joint usage of structured low-rank con-
502 straints and explicit phase mapping. Magn. Reson. Med. 89, 95–111.
503 doi:[10.1002/mrm.29422](https://doi.org/10.1002/mrm.29422).
- 504 Dai, E., Zhang, Z., Ma, X., Dong, Z., Li, X., Xiong, Y., Yuan, C., Guo, H.,
505 2018. The effects of navigator distortion and noise level on interleaved EPI
506 DWI reconstruction: a comparison between image- and *k*-space method.
507 Magn. Reson. Med. 80, 2024–2032. doi:[10.1002/mrm.27190](https://doi.org/10.1002/mrm.27190).
- 508 Dong, Z., Dai, E., Wang, F., Zhang, Z., Ma, X., Yuan, C., Guo, H., 2018.
509 Model-based reconstruction for simultaneous multislice and parallel imag-
510 ing accelerated multishot diffusion tensor imaging. Med. Phys. 45, 3196–
511 3204. doi:[10.1002/mp.12974](https://doi.org/10.1002/mp.12974).
- 512 Garyfallidis, E., Brett, M., Amirbekian, B., Rokem, A., van der Walt, S.,
513 Descoteaux, M., Nimmo-Smith, I., Contributors, D., 2014. DIPY, a library

- 514 for the analysis of diffusion MRI data. *Front. Neuroinform.* 8, 1–17. doi:[10.3389/fninf.2014.00008](https://doi.org/10.3389/fninf.2014.00008).
- 515
- 516 Grissom, W.A., Sacolick, L., Vogel, M.W., 2010. Improving high-field MRI
517 using parallel excitation. *Imaging Med.* 2, 675–693. doi:[10.2217/IIM.10.62](https://doi.org/10.2217/IIM.10.62).
- 517
- 518
- 519 Griswold, M.A., Jakob, P.M., Heidemann, R.M., Nittka, M., Jellus, V.,
520 Wang, J., Kiefer, B., Haase, A., 2002. Generalized autocalibrating par-
521 tially parallel acquisitions (GRAPPA). *Magn. Reson. Med.* 47, 1202–1210.
522 doi:[10.1002/mrm.10171](https://doi.org/10.1002/mrm.10171).
- 523
- 524 Guhaniyogi, S., Chu, M.L., Chang, H.C., Song, A.W., Chen, N.K., 2016. Mo-
525 tion immune diffusion imaging using augmented MUSE for high-resolution
526 multi-shot EPI. *Magn. Reson. Med.* 75, 639–652. doi:[10.1002/mrm.25624](https://doi.org/10.1002/mrm.25624).
- 527
- 528 Hammernik, K., Klatzer, T., Kobler, E., Recht, M.P., Sodickson, D.K., Pock,
529 T., Knoll, F., 2018. Learning a variational network for reconstruction of
530 accelerated MRI data. *Magn. Reson. Med.* 79, 3055–3071. doi:[10.1002/mrm.26977](https://doi.org/10.1002/mrm.26977).
- 531
- 532 Heidemann, R.M., Porter, D.A., Anwander, A., Feiweier, T., Heberlein, K.,
533 Knösche, T.R., Turner, R., 2010. Diffusion imaging in humans at 7 T
534 using readout-segmented EPI and GRAPPA. *Magn. Reson. Med.* 64, 9–
535 14. doi:[10.1002/mrm.22480](https://doi.org/10.1002/mrm.22480).
- 536
- 537 Hestenes, M.R., Stiefel, E., 1952. Methods of conjugate gradients for solving
538 linear systems. *J. Res. Natl. Bur. Stand.* 49, 409–436. doi:[10.6028/jres.049.044](https://doi.org/10.6028/jres.049.044).

- 537 Hu, Y., Wang, X., Tian, Q., Yang, G., Daniel, B., McNab, J., Hargreaves, B.,
538 2020. Multi-shot diffusion-weighted MRI reconstruction with magnitude-
539 based spatial-angular locally low-rank regularization (SPA-LLR). *Magn.*
540 *Reson. Med.* 83, 1596–1607. doi:[10.1002/mrm.28025](https://doi.org/10.1002/mrm.28025).
- 541 Huang, F., Vijayakumar, S., Li, Y., Hertel, S., Duensing, G.R., 2008. A soft-
542 ware channel compression technique for faster reconstruction with many
543 channels. *Magn. Reson. Imaging* 26, 133–141. doi:[10.1016/j.mri.2007.04.010](https://doi.org/10.1016/j.mri.2007.04.010).
- 545 Jeong, H.K., Gore, J.C., Anderson, A.W., 2013. High-resolution human
546 diffusion tensor imaging using 2-D navigated multishot SENSE EPI at 7
547 T. *Magn. Reson. Med.* 69, 793–802. doi:[10.1002/mrm.24320](https://doi.org/10.1002/mrm.24320).
- 548 Jones, D.K., 2010. Diffusion MRI: Theory, methods, and applications. Oxford
549 University Press. doi:[10.1093/med/9780195369779.001.0001](https://doi.org/10.1093/med/9780195369779.001.0001).
- 550 Katscher, U., Börnert, P., Leussler, C., van den Brink, J.S., 2003. Transmit
551 SENSE. *Magn. Reson. Med.* 49, 144–150. doi:[10.1002/mrm.10353](https://doi.org/10.1002/mrm.10353).
- 552 Knoll, F., Raya, J.G., Halloran, R.O., Baete, S., Sigmund, E., Bammer, R.,
553 Block, T., Otazo, R., Sodickson, D.K., 2015. A model-based reconstruction
554 for undersampled radial spin-echo DTI with variational penalties on the
555 diffusion tensor. *NMR Biomed* 28, 353–366. doi:[10.1002/nbm.3258](https://doi.org/10.1002/nbm.3258).
- 556 Lam, F., Li, Y., Peng, X., 2019. Constrained magnetic resonance spectro-
557 scopic imaging by learning nonlinear low-dimensional models. *IEEE Trans.*
558 *Med. Imaging* 39, 545–555. doi:[10.1109/TMI.2019.2930586](https://doi.org/10.1109/TMI.2019.2930586).

- 559 Le Bihan, D., Breton, E., Lallemand, D., Grenier, P., Cabanis, E., Laval-
560 Jeantet, M., 1986. MR imaging of intravoxel incoherent motions: appli-
561 cation to diffusion and perfusion in neurologic disorders. Radiology 161,
562 401–407. doi:[10.1148/radiology.161.2.3763909](https://doi.org/10.1148/radiology.161.2.3763909).
- 563 Liang, Z.P., 2007. Spatiotemporal imaging with partially separable functions,
564 in: 2007 4th IEEE International Symposium on Biomedical Imaging: From
565 Nano to Macro, pp. 988–991. doi:[10.1109/ISBI.2007.357020](https://doi.org/10.1109/ISBI.2007.357020).
- 566 Liu, C., Moseley, M.E., Bammer, R., 2005. Simultaneous phase cor-
567 rection and SENSE reconstruction for navigated multi-shot DWI with
568 non-Cartesian k -space sampling. Magn. Reson. Med. 54, 1412–1422.
569 doi:[10.1002/mrm.20706](https://doi.org/10.1002/mrm.20706).
- 570 Lustig, M., Donoho, D., Pauly, J.M., 2007. Sparse MRI: The application of
571 compressed sensing for rapid MR imaging. Magn. Reson. Med. 58, 1182–
572 1195. doi:[10.1002/mrm.21391](https://doi.org/10.1002/mrm.21391).
- 573 Mani, M., Jacob, M., Kelley, D., Magnotta, V., 2017. Multi-shot sensitivity-
574 encoded diffusion data recovery using structured low-rank matrix comple-
575 tion (MUSSELS). Magn. Reson. Med. 78, 494–507. doi:[10.1002/mrm.26382](https://doi.org/10.1002/mrm.26382).
- 577 Mani, M., Magnotta, V.A., Jacob, M., 2021. qModeL: A plug-and-play
578 model-based reconstruction for highly accelerated multi-shot diffusion MRI
579 using learned priors. Magn. Reson. Med. 86, 835–851. doi:[10.1002/mrm.28756](https://doi.org/10.1002/mrm.28756).

- 581 Mansfield, P., 1977. Multi-planar image formation using NMR spin echoes.
- 582 J Phys C 10, 55–58. doi:[10.1088/0022-3719/10/3/004](https://doi.org/10.1088/0022-3719/10/3/004).
- 583 Maudsley, A.A., 1980. Multiple-line-scanning spin density imaging. J. Magn.
- 584 Reson. 41, 112–126. doi:[10.1016/0022-2364\(80\)90207-3](https://doi.org/10.1016/0022-2364(80)90207-3).
- 585 Merboldt, K.D., Hanicke, W., Frahm, J., 1985. Self-diffusion NMR imaging using stimulated echoes. J. Magn. Reson. 64, 479–486. doi:[10.1016/0022-2364\(85\)90111-8](https://doi.org/10.1016/0022-2364(85)90111-8).
- 588 Mori, S., Crain, B.J., Chacko, V.P., Van Zijl, P.C.M., 1999. Three-dimensional tracking of axonal projections in the brain by magnetic resonance imaging. Ann. Neurol. 45, 265–269. doi:[10.1002/1531-8249\(199902\)45:2<265::AID-ANA21>3.0.CO;2-3](https://doi.org/10.1002/1531-8249(199902)45:2<265::AID-ANA21>3.0.CO;2-3).
- 592 Ong, F., Lustig, M., 2019. SigPy: A Python package for high performance iterative reconstruction, in: Proceedings of the 27th Annual Meeting of
- 593 ISMRM, Montréal, CAN, p. 4819. doi:[10.5281/zenodo.5893788](https://doi.org/10.5281/zenodo.5893788).
- 595 Ong, F., Zhu, X., Cheng, J.Y., Johnson, K.M., Larson, P.E.Z., Vasanawala, S.S., Lustig, M., 2020. Extreme MRI: Large-scale volumetric dynamic
- 596 imaging from continuous non-gated acquisitions. Magn. Reson. Med. 84,
- 597 1763–1780. doi:[10.1002/mrm.28235](https://doi.org/10.1002/mrm.28235).
- 599 Pipe, J.G., Farthing, V.G., Forbes, K.P., 2002. Multishot diffusion-weighted
- 600 FSE using PROPELLER MRI. Magn. Reson. Med. 47, 42–52. doi:[10.1002/mrm.10014](https://doi.org/10.1002/mrm.10014).
- 602 Polak, D., Splitthoff, D.N., Clifford, B., Lo, W.C., Huang, S.Y., Conklin, J.,
- 603 Wald, L.L., Setsompop, K., Cauley, S., 2022. Scout accelerated motion

- 604 estimation and reduction (SAMER). Magn. Reson. Med. 87, 163–178.
605 doi:[10.1002/mrm.28971](https://doi.org/10.1002/mrm.28971).
- 606 Porter, D.A., Heidemann, R.M., 2009. High resolution diffusion-weighted
607 imaging using readout-segmented echo-planar imaging, parallel imaging
608 and a two-dimensional navigator-based reacquisition. Magn. Reson. Med.
609 62, 468–475. doi:[10.1002/mrm.22024](https://doi.org/10.1002/mrm.22024).
- 610 Pruessmann, K.P., Weiger, M., Scheidegger, M.B., Boesiger, P., 1999.
611 SENSE: Sensitivity encoding for fast MRI. Magn. Reson. Med. 42, 952–
612 962. doi:[10.1002/\(SICI\)1522-2594\(199911\)42:5<952::AID-MRM16>3.0.CO;2-S](https://doi.org/10.1002/(SICI)1522-2594(199911)42:5<952::AID-MRM16>3.0.CO;2-S).
- 613
- 614 Ra, J.B., Rim, C.Y., 1993. Fast imaging using subencoding data sets from
615 multiple detectors. Magn. Reson. Med. 30, 142–145. doi:[10.1002/mrm.1910300123](https://doi.org/10.1002/mrm.1910300123).
- 617 Roemer, P.B., Edelstein, W.A., Hayes, C.E., Souza, S.P., Mueller, O.M.,
618 1990. The NMR phased array. Magn. Reson. Med. 16, 192–225. doi:[10.1002/mrm.1910160203](https://doi.org/10.1002/mrm.1910160203).
- 620 Setsompop, K., Fan, Q., Stockmann, J., Bilgic, B., Huang, S., Cauley, S.F.,
621 Nummenmaa, A., Wang, F., Rathi, Y., Witzel, T., Wald, L.L., 2018. High-
622 resolution *in vivo* diffusion imaging of the human brain with generalized
623 slice dithered enhanced resolution: Simultaneous multislice (gSlider-SMS).
624 Magn. Reson. Med. 79, 141–151. doi:[10.1002/mrm.26653](https://doi.org/10.1002/mrm.26653).
- 625 Setsompop, K., Gagoski, B.A., Polimeni, J.R., Witzel, T., Wedeen, V.J.,
626 Wald, L.L., 2012. Blipped-controlled aliasing in parallel imaging for si-

- 627 multaneous multislice echo planar imaging with reduced *g*-factor penalty.
628 Magn. Reson. Med. 67, 1210–1224. doi:[10.1002/mrm.23097](https://doi.org/10.1002/mrm.23097).
- 629 Shafieizargar, B., Jeurissen, B., Poot, D.H.J., Klein, S., Van Audekerke,
630 J., Verhoye, M., den Dekker, A.J., Sijbers, J., 2023. ADEPT: Accurate
631 diffusion echo-planar imaging with multi-contrast shoTs. Magn. Reson.
632 Med. 89, 396–410. doi:[10.1002/mrm.29398](https://doi.org/10.1002/mrm.29398).
- 633 Tournier, J.D., Smith, R., Raffelt, D., Tabbara, R., Dhollander, T., Pietsch,
634 M., Christiaens, D., Jeurissen, B., Yeh, C.H., Connelly, A., 2019. MRtrix3:
635 A fast, flexible and open software framework for medical image processing
636 and visualisation. NeuroImage 202, 116137. doi:<https://doi.org/10.1016/j.neuroimage.2019.116137>.
- 638 Trzasko, J., Manduca, A., 2011. Local versus global low-rank promotion in
639 dynamic MRI series reconstruction, in: Proceedings of the 19th Annual
640 Meeting of ISMRM, Montréal, CAN, p. 4371.
- 641 Tuch, D.S., Reese, T.G., Wiegell, M.R., Makris, N., Belliveau, J.W., Wedeen,
642 V.J., 2002. High angular resolution diffusion imaging reveals intravoxel
643 white matter fiber heterogeneity. Magn. Reson. Med. 48, 577–582. doi:[10.1002/mrm.10268](https://doi.org/10.1002/mrm.10268).
- 645 Uecker, M., Lai, P., Murphy, M.J., Virtue, P., Elad, M., Pauly, J.M.,
646 Vasanawala, S.S., Lustig, M., 2014. ESPIRiT – an eigenvalue approach
647 to autocalibrating parallel MRI: Where SENSE meets GRAPPA. Magn.
648 Reson. Med. 71, 990–1001. doi:[10.1002/mrm.24751](https://doi.org/10.1002/mrm.24751).

- 649 Wu, W., Koopmans, P.J., Andersson, J.L., Miller, K.L., 2019. Diffusion
650 Acceleration with Gaussian process Estimated Reconstruction (DAGER).
651 Magn. Reson. Med. 82, 107–125. doi:[10.1002/mrm.27699](https://doi.org/10.1002/mrm.27699).
- 652 Wu, W., Miller, K.L., 2017. Image formation in diffusion MRI: A review
653 of recent technical developments. J. Magn. Reson. Imaging 46, 646–662.
654 doi:[10.1002/jmri.25664](https://doi.org/10.1002/jmri.25664).
- 655 Zhang, T., Pauly, J.M., Levesque, I.R., 2015. Accelerated parameter mapping
656 with a locally low rank constraint. Magn. Reson. Med. 73, 655–661. doi:[10.1002/mrm.25161](https://doi.org/10.1002/mrm.25161).

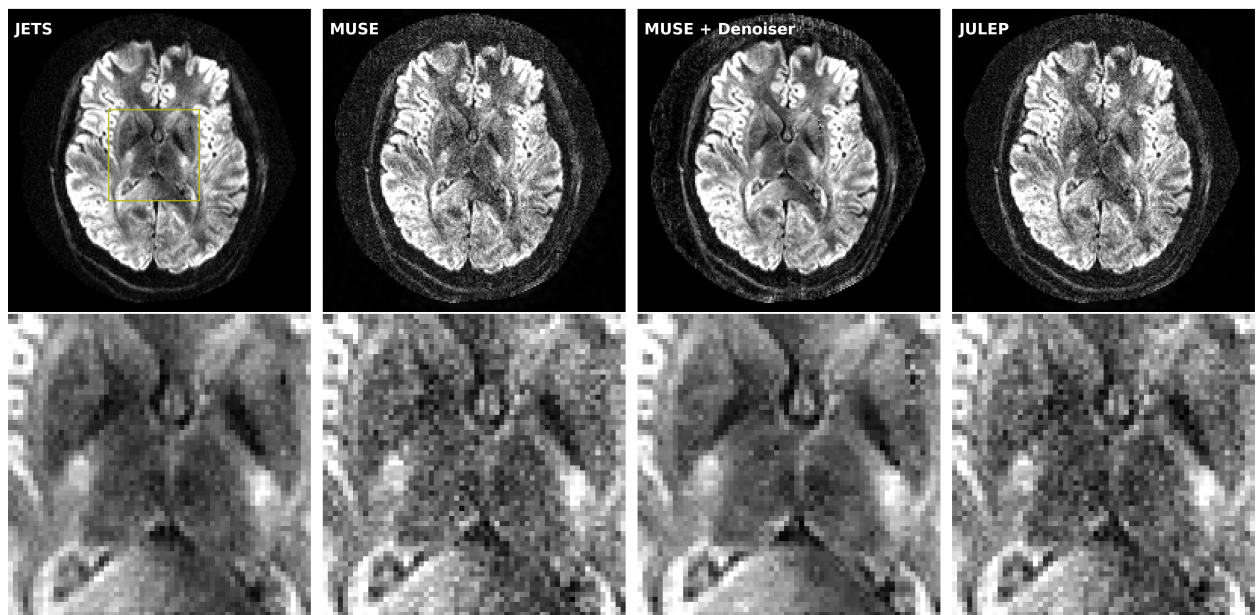
Supplementary Information

Accelerated Diffusion Weighted Magnetic Resonance Imaging at 7 T: Joint Reconstruction for Shift-Encoded Navigator-based Interleaved Echo Planar Imaging (JETS-NAViEPI)

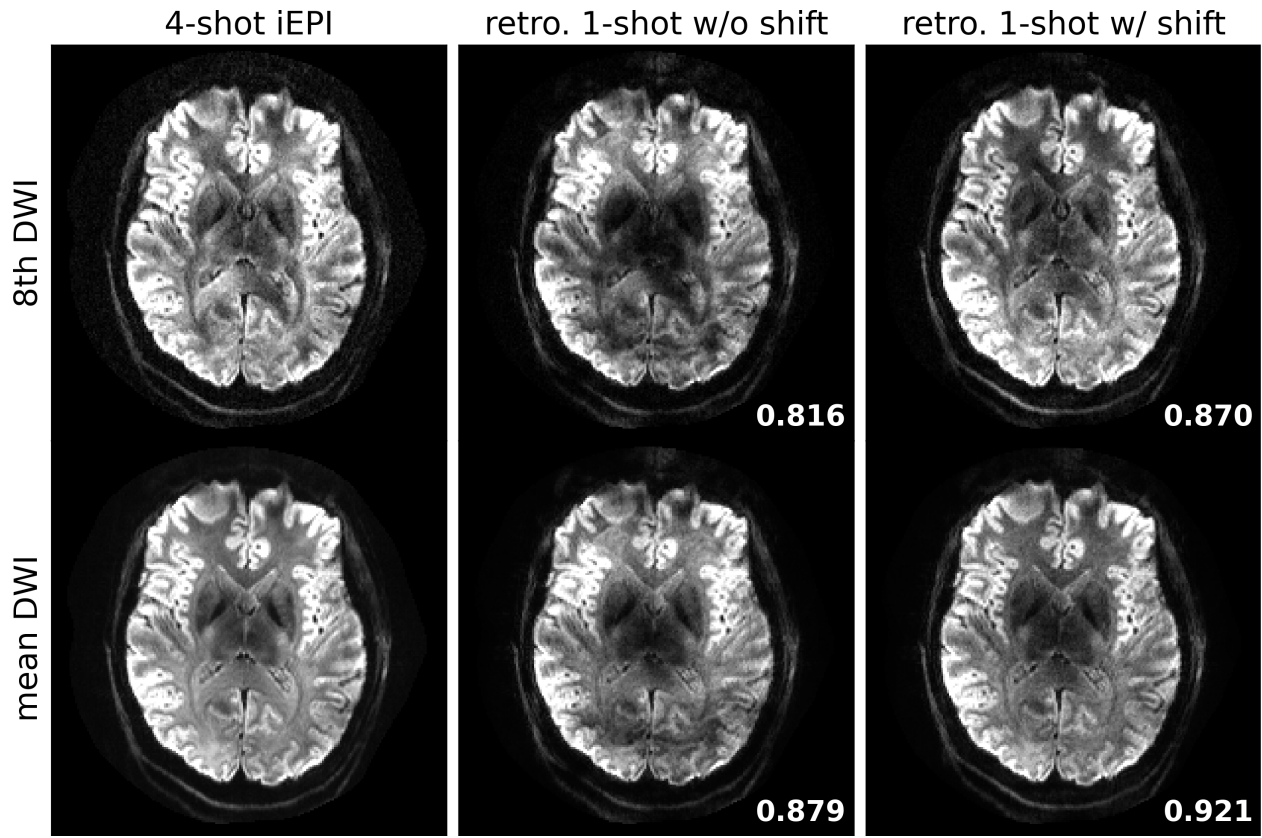
Zhengguo Tan, Patrick A. Liebig, Robin M. Heidemann, Frederik B. Laun, Florian Knoll

Here we aim to reproduce the results. Another subject with informed consent was recruited and measured by all protocols listed in Table 1 in the main manuscript.

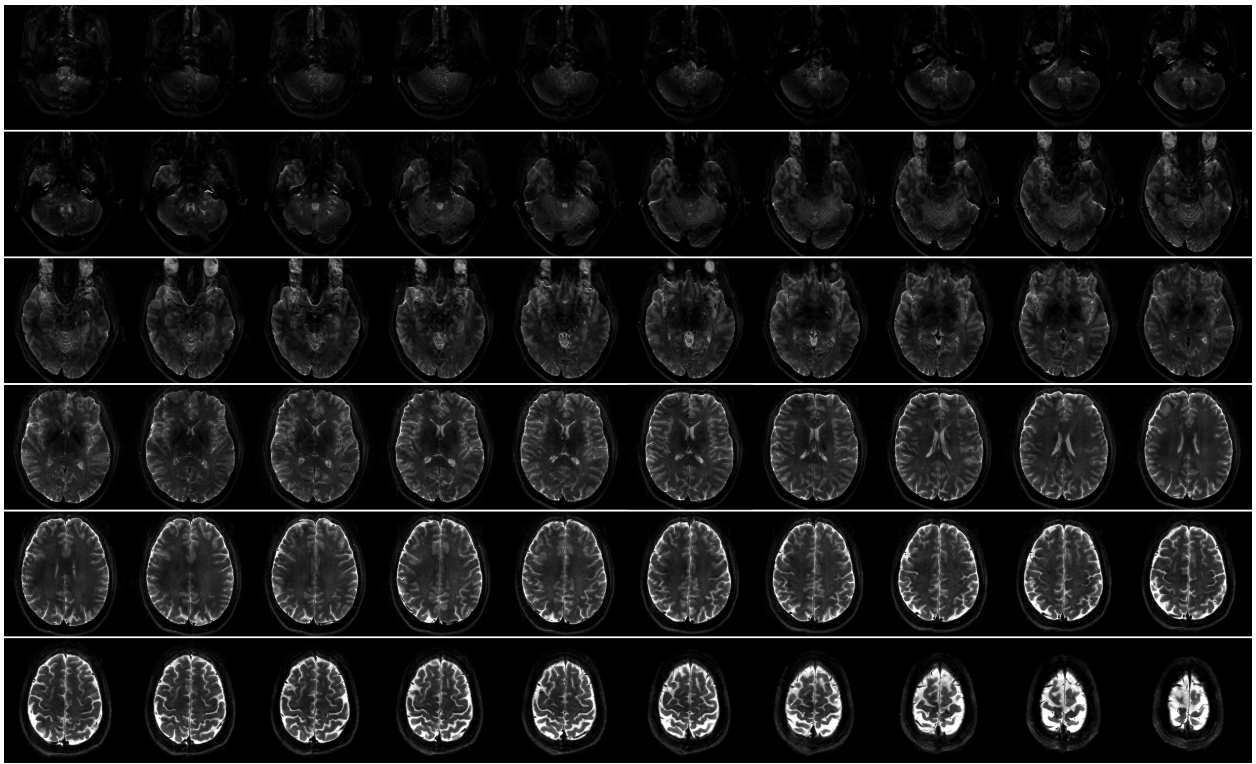
8th DW image from 4-shot iEPI @ 1 mm ISO



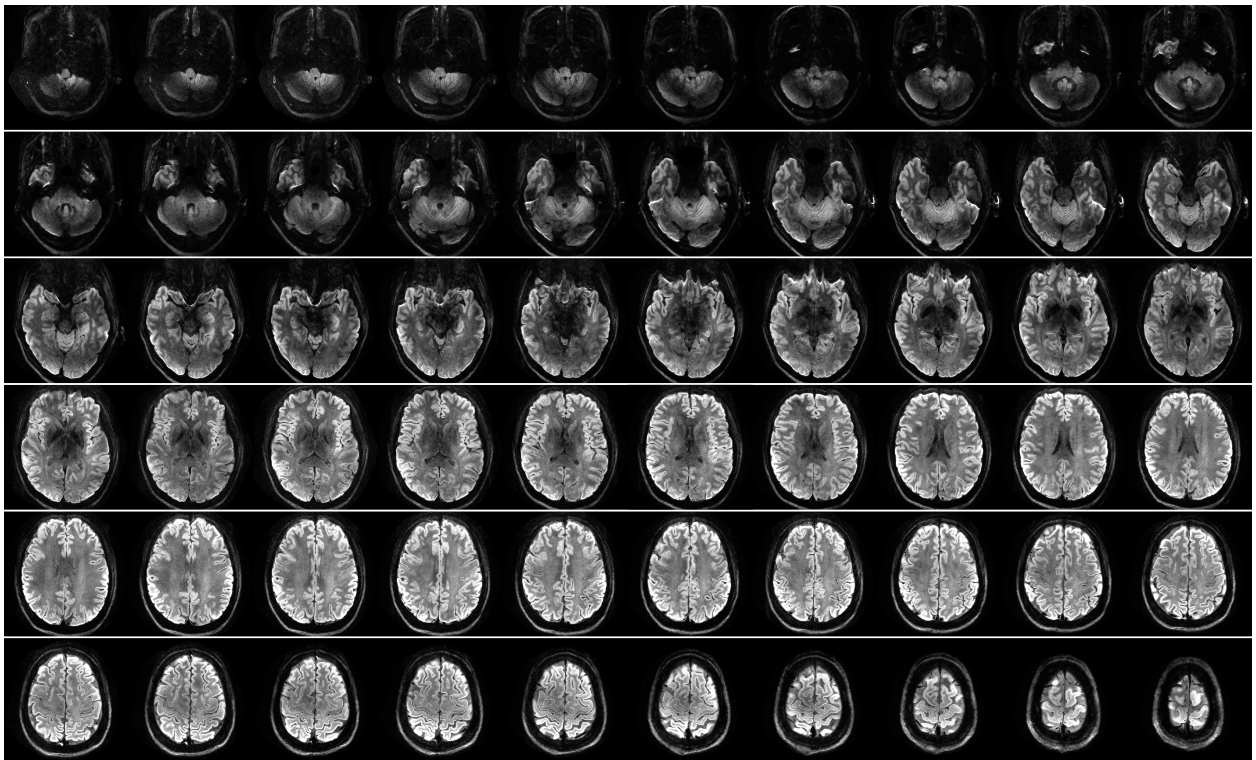
SI Figure S1: Reproducing Protocol #1. Reconstructed DW images (the 8th diffusion encoding) based on 4-shot iEPI acquisition with 1 mm isotropic resolution. Four reconstruction methods are compared (from left to right): JETS, MUSE, MUSE with denoiser, and JULEP. The 2nd row displays the magnified views of the yellow square.



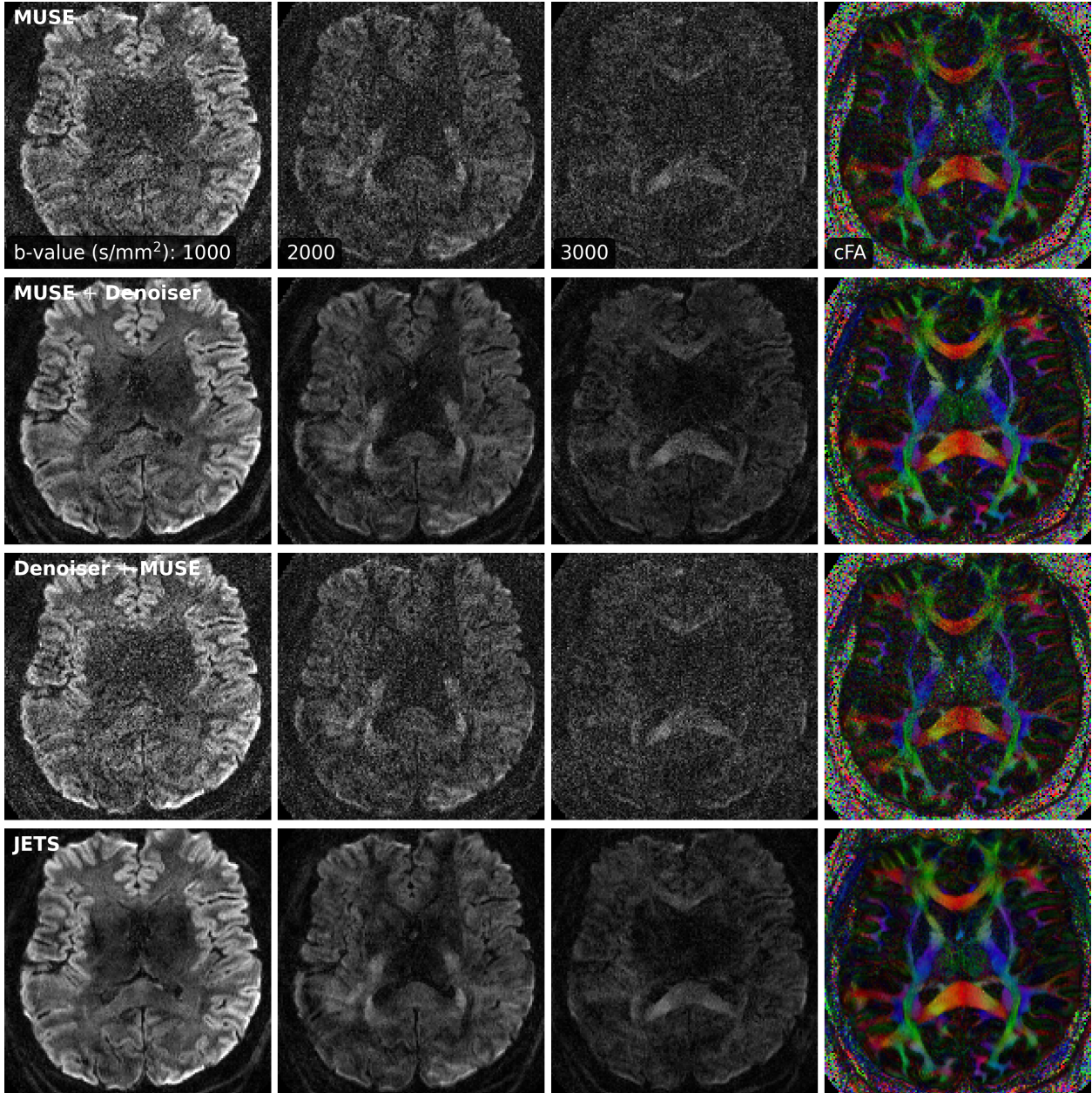
SI Figure S2: Reproducing Protocol #1. Quantitative validation of the proposed k_y -shift encoding sampling pattern based on 4-shot iEPI acquisition with 1 mm isotropic resolution. (Top) the 8th diffusion encoding and (bottom) mean DWI over 20 diffusion encodings. (1st column) JETS reconstruction of 4-shot iEPI acquisition is used as the ground truth. The 2nd and the 3rd column displays JETS reconstruction of retrospectively undersampled 1-shot acquisition without and with k_y shifting, respectively.



SI Figure S3: Reproducing Protocol #3. Reconstructed b_0 images from the 3-scan trace acquisition with the voxel size $0.5 \times 0.5 \times 2.0 \text{ mm}^3$.



SI Figure S4: Reproducing Protocol #3. Reconstructed TRACE images from the 3-scan trace acquisition with the voxel size $0.5 \times 0.5 \times 2.0 \text{ mm}^3$.



SI Figure S5: Reproducing Protocol #2. The FOV and bandwidth were adapted as 200 mm and 1086 Hz/pixel, respectively. Comparison of three-shell DWIs and cFA maps reconstructed by (top to bottom) MUSE, MUSE with the local-PCA denoiser, MUSE with the local-PCA denoiser applied before the multi-shot combination, and the proposed JETS method, respectively. The local-PCA denoiser, when applied to shot images (3rd row), is less effective compared to its application to shot-combined images (2nd row). The reason is that shot images are reconstructed from the central k -space data, and thus have coarse resolution.

Imaging Neuroscience #203: Responses to Editors and Reviewers

Reviewer #989

I thank the Authors for responding to all of my comments.

Thank you for your review.

Some minor points:

- 1) *I think it would be good to have a mention in the Materials and Methods section of the replication that you put in the Supplementary Information to make readers aware it is there.*

Done.

- 2) *Perhaps I missed it, but I did not see it stated whether the participant in the Supplementary Information gave informed consent. I would suggest adding a statement confirming informed consent was given in the Supplementary Information.*

Done.

- 3) *Fig. 6: Description of what the arrows mean is missing from caption.*

Done.

- 4) *pg. 30: "Alternatively, the multi-echo acquisition could be used..." should I think be "Alternatively, a multi-echo acquisition could be used..."*

Done.

Reviewer #990

Authors have partially addressed my previous comments. A list of pending issues is listed below:

Major:

- 3.b.1) Sorry, still cannot see any particular limitation for applying denoising before shot combination in MUSE. Shot reconstructions for all diffusion measures from MUSE could be concatenated and PCA applied before multi-shot combination. I invite to consider testing this approach as well (if not appropriate, please provide reasons for not doing / state as future line).

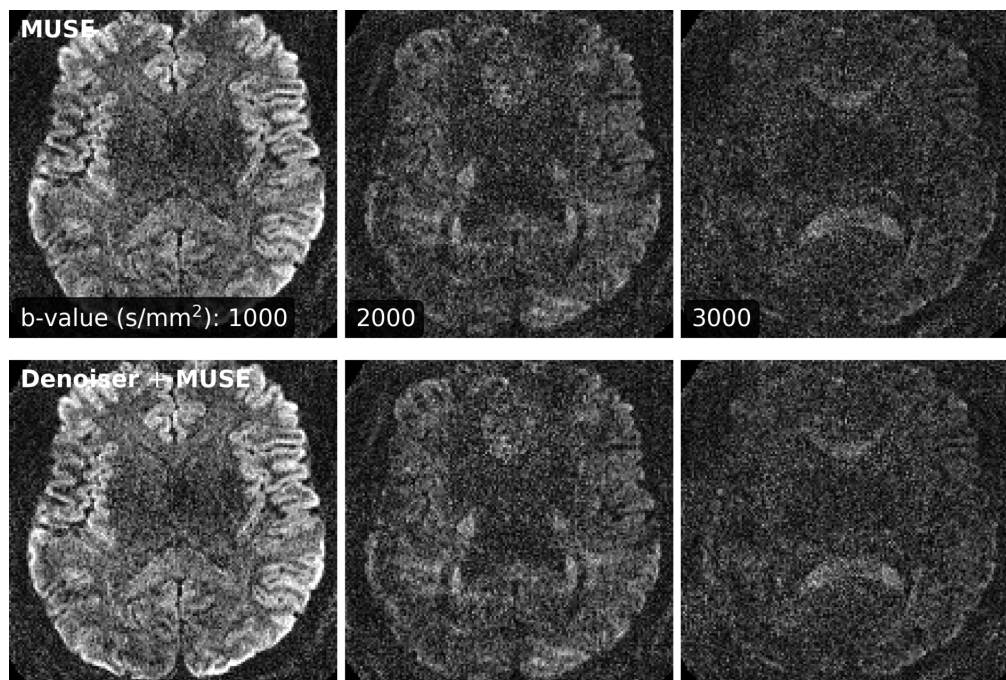


Figure 1: Comparison of three-shell DWIs with data acquired by Protocol #1 in Table 1. (Top) The standard MUSE reconstruction. (Bottom) The MUSE reconstruction with the local PCA denoiser applied before the multi-shot combination.

Thank you for the question. We applied the local PCA denoiser before multi-shot combination, and compared the results with the standard MUSE without PCA before multi-shot combination. The final reconstructed DWIs exhibit no major difference between these two approaches, as shown in Figure 1. Shot images are reconstructed from the central k -space data, and thus have coarse resolution. As a result, the local PCA denoiser, when applied to the shot images, is less effective compared to its application to full-resolution shot-combined images. We included this result in both Figure 9 in the manuscript and Figure S5 in Supplementary Information.

- 3.b.2) Discussion on synergies between LLR and local PCA may be misleading. Authors mention that the "denoiser performs hard thresholding" but the cited approach is actually performing "singular value shrinkage", not thresholding (see first line of abstract). "use of LLR regular-

ization for image reconstruction followed by the denoiser as a post-processing step” → but these are closely related methods based on similar principles, so why a substantial benefit to be expected in applying one on top of another?, why not fusing them trying to get the best of both? I think that discussion should focus on synergies rather than seeing them as separate steps.

Thank you for the suggestion. We rewrote this paragraph and focused more on synergies.

- 4.a) *I don't think this is properly attended. In Fig. 6 you refer to block sizes of 3, 6 and 9, which is not matched to widths of 1, 2 and 4 as block size is square of width. Note 6 is also mentioned in text as baseline block size, which also seems erroneous. Also, in new text, "This observation agrees with the suggestion that the patch size should be no smaller than and close to the diffusion directions (Cordero-Grande et al., 2019)." But in (Cordero-Grande et al., 2019), patch sizes are automatically estimated. Have looked again for reported suggestion in the manuscript without success. Also, whilst patch sizes inducing close to square matrices could be intuitively better for large matrices, that's not so clear for small matrices as here (4 columns). Thus, usage of this motivating sentence seems rather speculative / forced, so sentence could be deleted or else further details should be provided. See also related minor point 9.*

Thank you for pointing this out. We delete the sentence in the manuscript.

- 4.b) *L. 314 Please report meaning of "partially overlapping" (i.e., specific parameters of overlap) and also meaning of red arrows in Fig. 6.*

Done.

- 7) *Please, explicitly include criteria for slice / diffusion encoding selection in the manuscript for Figs. 4-9 (including further clarifications to those provided in response for Figs. 7 and 9).*

Done.

Minor:

- 9) *I appreciate authors efforts to clarify this issue. Unfortunately, new results raise an important previously hidden issue. From Figure 1 in Responses to Editors and Reviewers, seems a normalization of singular values by block width would produce more comparable thresholds. This normalization is commonly used to counteract normalized eigenvectors with variable lengths. If agreed, experiments should be repeated by proper normalization of singular values, and modifications performed to methods presentation, including novel thresholds reporting. Please provide a detailed list of changes in your response. Otherwise, please explain why this normalization is not appropriate. This is related also to some of the concerns in major point 4, as, without proper normalization, optimal patch size is mainly driven by adequacy of preset threshold.*

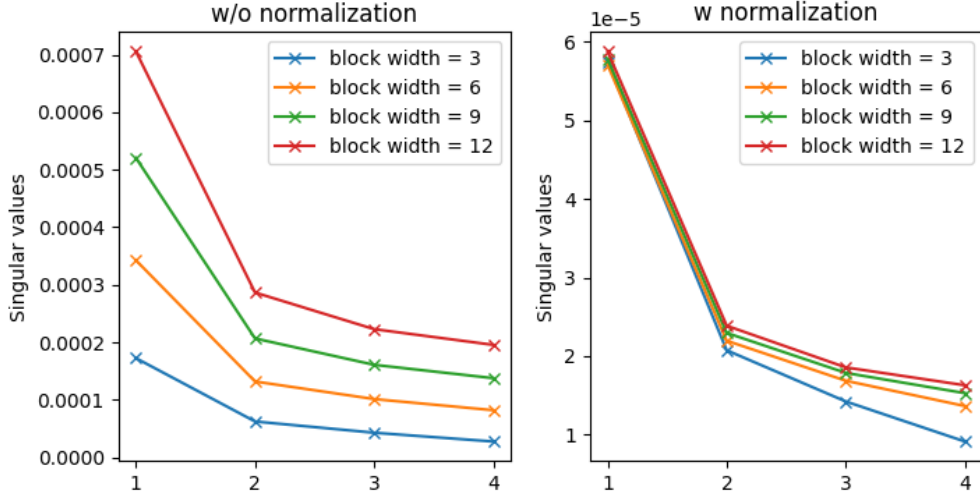


Figure 2: Comparison of singular values (left) without and (right) with normalization.

Very good observation. Following your suggestion, we added the normalization option. As shown in Figure 2, the normalization (i.e., division of singular values by the corresponding block width) does normalize the largest eigenvalue, but shows small deviations in other eigenvalues.

In the LLR denoising function, we first divide the singular values by the block width, perform singular value soft thresholding, and then multiply the thresholded singular values with the block width. As shown in Figure 3, this normalization strategy does not render the same denoising effect for different block widths. This can be identified in the difference image from the block width of 9, which shows residual structural edges, whereas the difference image from the block width of 3 does not. Moreover, note that the soft thresholding is a nonlinear operator. Thus, the normalization strategy is not balanced and scales the thresholded singular values.

Please refer to https://github.com/ZhengguoTan/demo_jets_diffusion_mri_7t/blob/main/demo_llr.ipynb for the implementation and the interactive demo.

- 12) *Thanks, unclear why this needs to be iterative rather than controlled by single filtering step parameters. Also, from eq. 6 you'd be smoothing the magnitude as well, not only the phase, so presentation of this equation may require modifications. Please, explain and report how you choose the number of iterations.*

Very good point, and thank you for the suggestion. First, we found out that the iterative procedure in Eq. 6, $\mathbf{x}^{(k+1)} = \mathbf{F}^{-1}\mathcal{H}\mathbf{F}\mathbf{x}^{(k)}$, is equivalent to setting a single filtering parameter, $\mathbf{x} = \mathbf{F}^{-1}\mathcal{H}^K\mathbf{F}\mathbf{x}$ with K the number of iterations. Second, as shown in Figures 4 and 5, the scalar exponent K controls the width of the filter. A larger K renders a narrower filter width. Consequently, the shot phases without filtering ($K = 0$) show ripple-like artifacts, whereas aggressive filtering (e.g., $K = 160$) removes shot-to-shot phase variation. Therefore, We chose $K = 5$ in this work.

Single-direction DWI with normalization

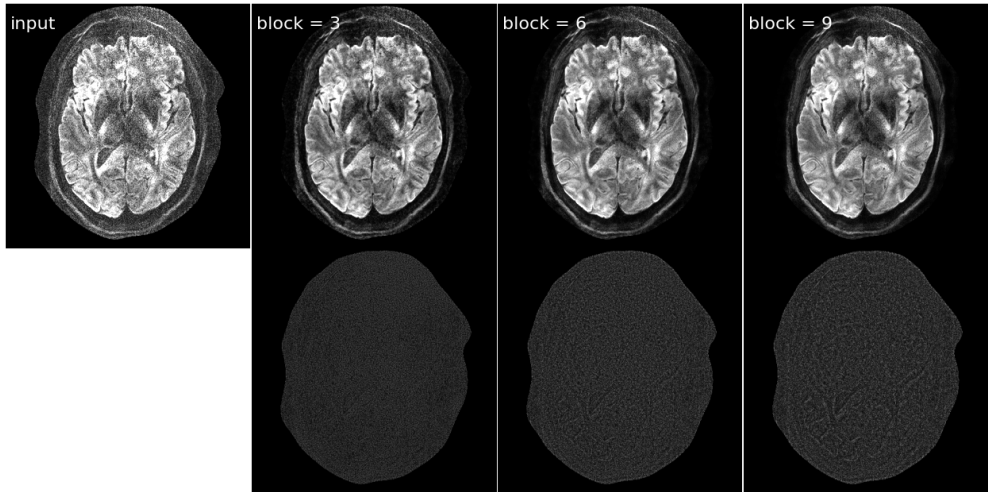


Figure 3: LLR denoising with normalization. (Top) The first image shows the input to the denoiser. The other three images show the denoised output with different block widths. (Bottom) The difference between the input and the denoised outputs.

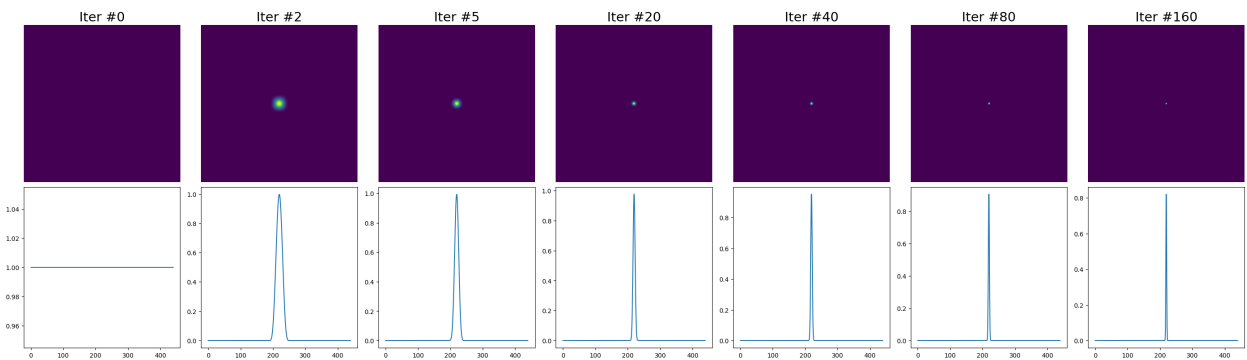


Figure 4: (Top) Filters as a function of the iteration number K . (Bottom) Line profiles crossing the center of corresponding filters.

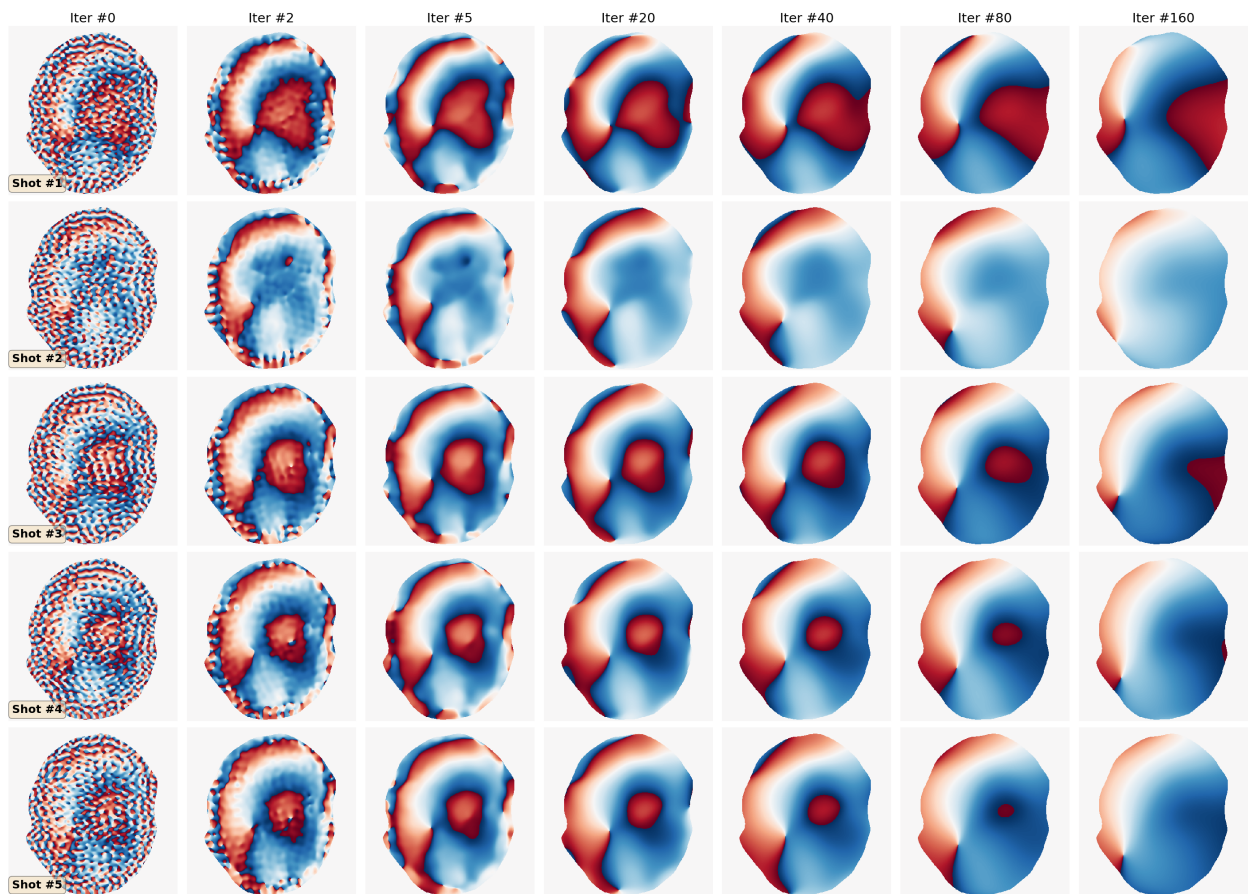


Figure 5: Filtered shot phases with varying scalar exponents K .

13) (New content) L369 "the multi-echo" → "a multi-echo".

Done.